Available online at www.sciencedirect.com

SciVerse ScienceDirect

Procedia Engineering 00 (2012) 000–000

Procedia Engineering

www.elsevier.com/locate/procedia

5th BSME International Conference on Thermal Engineering

Analysis of electrolyte flow in localized electrochemical deposition

Mohammad Ahsan Habib[a,*], Mustafizur Rahman[b]

[a]*Department Mechanical and Chemical Engineering, Islamic University of Technology (IUT), Bangladesh*
[b]*Department Mechanical Engineering, National University of Technology (NUS), Singapore*

Abstract

Localized electrochemical deposition (LECD) is a favorable technology for fabrication of the high-aspect ratio electrodes of various materials. This technology is found to be one of the simple and inexpensive ways to fabricate non-circular electrodes for micro-EDM. In order to fabricate non-circular electrodes a mask of non-conductive material is placed between the anode and cathode, which is immersed in a mixed electrolyte of copper sulfate, 1.0M sulfuric acid and as an additive agent 0.04 gm/liter of thiourea. The deposition of copper is localized on the cathode surface using a mask and applying ultra-short voltage pulses between the anode and cathode. In this set up the cathode is placed above the anode and mask, so that the deposited electrode can be used directly for EDM or any application without changing its orientation. In order to localize the deposited structure on the cathode surface, the electrolyte needs to flow through the mask and needs to touch the cathode and a constant flow rate of the electrolyte is maintained by using a pump. For this reason, micro holes of desired shapes are fabricated in the mask using micro milling. This study shows the effect of electrolyte flow through the micro holes of the mask and micro gap between the mask and anode on the microstructure of deposited electrode using FLUENT analysis. Moreover, an optimum range of electrolyte flow rate through the micro passages is also shown for the LECD process in order to fabricate high aspect ratio microstructures.

Keywords: Localized electrochemical deposition, LECD, Electrolyte, Micro holes, Micro gap, FLUENT.

1. Introduction

Currently new micro-fabrication processes are being been investigated worldwide to build micro electromechanical structure such as gears, springs, helices and columns and these are required for the apprehension of miniature micro machine that can access spaces never before explored by human beings. In order to handle this challenge fabrication techniques related to material deposition such as low-pressure chemical vapor deposition (LPCVD), laser-assisted chemical vapor deposition (LCVD), plasma-enhanced chemical vapor deposition (PECVD), ultraviolet stereo lithography, spinning, spraying and localized electrochemical deposition (LECD) are being used presently [1].

About a decade ago, as a practical technique for inexpensive free form micro-fabrication, the LECD process has a huge prospective to afford solutions to a variety of challenges [2]. Madden and Hunter are the first researchers to introduce the LECD process for microfabrication of the three dimensional metal structures [3]. Jansson et al. had tested the LECD process with different kinds of nickel plating solutions to deposit the nickel structures [4]. El-Giar et al. had used the same method to deposit the long thin micrometer-size copper columns, copper electrical inter-connects and tips for scanning probe

* Corresponding author. Tel.: +8801742017332; fax: +880 2 9291260.
E-mail address: mahabib@iut-dhaka.edu

microscopy applications [5,6]. Yeo et al. investigated the deposition phenomena of LECD for Ni micro column structure by using open-loop (without analog feedback) and closed loop (with analog feedback) systems [7]. Besides, the investigations have also done on the effect of rotational electrode on the growth of nickel micro column structure [8], and the effect of ultrasonic vibration on the rate of deposition, concentration and porosity of the nickel micro columns [9]. Most of the researches have used the copper as a substrate and the platinum as a counter electrode to fabricate a column structure in the LECD process. A new LECD process is implemented by Habib et al. [1, 10-11] to fabricate the complex cross-sectional shape of electrodes where the coppers are used for both substrate and counter electrode. The masks which are made from non-conductive materials and with different designs are used to provide the pre-shape for the deposition purpose. The substrate is located on the machine z-axis which is above the counter electrode because of it eases to proceed to EDM process directly just after the deposition. By applying this method, the electrode clamping error can be minimized and the production rate can be increased.

In order to increase the aspect ratio of the electrode, close loop control of the LECD process is required, where the effect of electrolyte flow plays a significant role. In this study, a detail electrolyte flow analysis is studied and a range of operational parameters are presented. It can be also seen that using these parameters a high aspect ratio micro electrode is fabricated and micro-EDM is also done by using that micro-electrode.

2. Concept and Structural construction of LECD and EDM combine setup

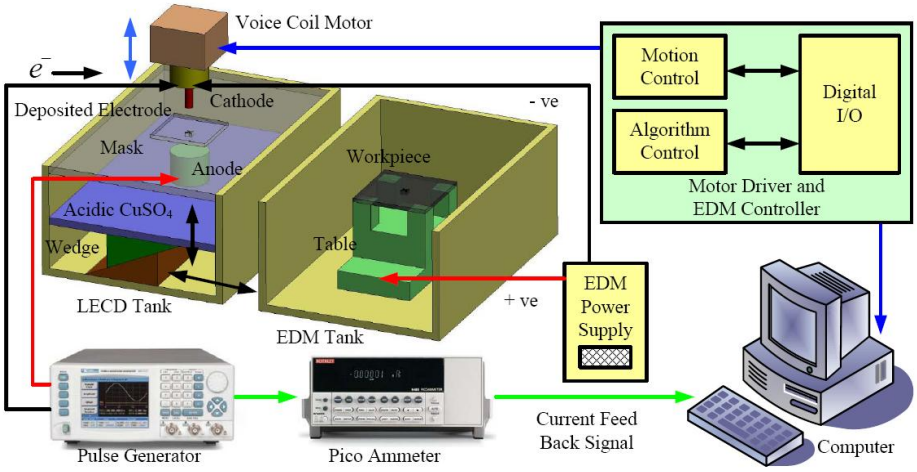

Fig. 1. Schematic diagram of LECD and EDM combine setup

In the experimental setup, two separate sub-setups are used one for LECD and another for EDM operation. Both of them are mounted on a 3-axes multi-process machine and figure 1 and 2 show the structure of desktop machine.

The LECD sub-setup consists of two main parts: a cathode electrode holder and a deposition tank. In this process the metallic ion can become solid metal and deposited on the cathode surface if sufficient amount of electric current pass through an electrolyte or plating solution. Solution that contains charged ions known as electrolyte or plating solution. These positively charged ions can be achieved by dissolving metallic salt into water. The acidic supper sulfate is used as an electrolyte and an anode is immersed in this electrolyte. Cathode is placed above the anode and between the anode and cathode a non-conductive mask is located to create the non-circular shape of the deposition. The mask is made from a non-conductive material like PMMA (Poly methyl methacrylate). A small constant gap is maintained between the anode and mask during deposition time using a micrometer screw. When both of the electrodes are conducted electrically, current will pass through the plating solution. The positively charges metal ions get (Cu^{2+}) deposited as solid metal on the cathode through the non-conductive mask. The through hole of different shape (X shape, Y shape, O shape etc.) of the mask is prepared by micro-milling operation. A more realistic equation is

$$Cu^{2+} + 2e^{-} \rightarrow Cu \downarrow \text{ (Cathode)} \qquad H_2O \rightarrow 2H^{+} + 2e^{-} + \frac{1}{2}O_2 \uparrow \text{ (Anode)}$$

For electrode deposition pure copper is used for both the base material where the metal will be deposited and anode material. For electrode surface finish it is required to polish surface by the successive grade of 600, 1200, 1500 and 2000 silicon carbide papers. Finally, to obtain a smooth and mirror surface a final fine polishing was done by 1.0μm diamond paste on nylon cloth. In the EDM sub-setup a workpiece fixing table is used to fix the workpiece which is kept inside an

EDM tank and the dielectric is supplied in the working area with the help of a nozzle. Finally, the deposited electrode which is attached with the voice coil motor can do the EDM without changing the tool position.

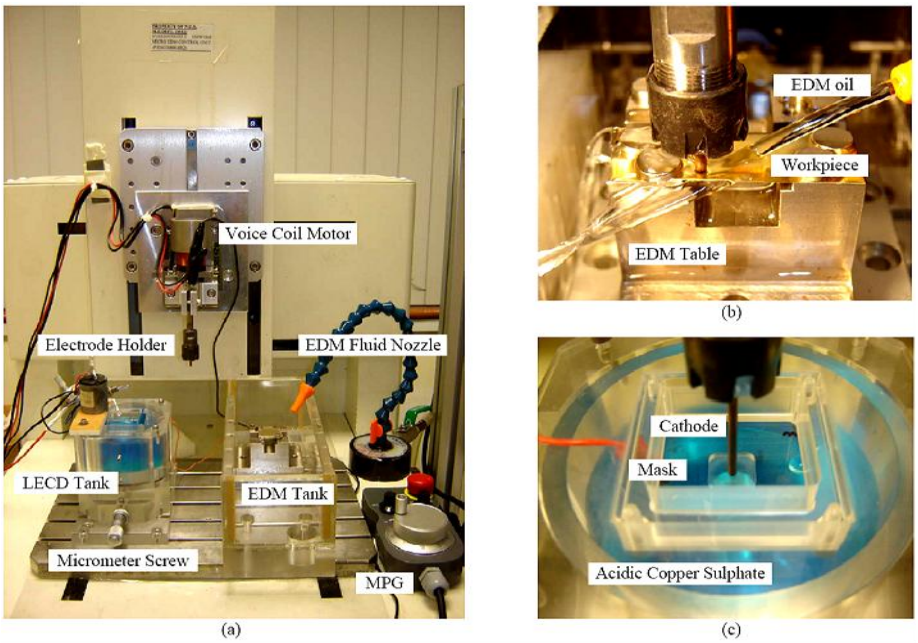

Fig. 2. (a) LECD and EDM setup (b) LECD operation running (c) EDM operation running

3. Results and Discussions

3.1. Process modeling and simulation

When a cathode and an anode are immersed in a solution, an interface consists of two equal and opposite layers of charge, one on the metal and other in solution is created. This pair of charged layers, called the double layer, is equivalent to a parallel plate capacitor. The variation of potential in the double layer with the distance from the electrode is linear. On both the electrode surface the electro chemical double layer forms a capacitor. This double layer is charged when a potential is applied between the two electrodes. The charging time constant (τ_c) for the double layer is the product of resistance (R) and capacitance (c_{DL}). The charging current has to flow through the electrolyte, whose resistance is proportional to the length of the current path; that is, the distance between the electrodes (d_{gap}). Therefore, resistance is the product of the gap distance between the electrodes (d_{gap}) and the specific electrolyte resistivity (ρ). Finally, the time constant:

$$\tau_C = R \times C = \rho . c_{DL} . d_{gap} \tag{1}$$

The charged potential of a double layer at any time (t):

$$\varphi_C = \varphi_0 \left(1 - e^{-\frac{t}{\tau_C}} \right) \approx \varphi_0 \frac{t}{\tau_C} \tag{2}$$

When plus voltage is applied, there is no electrochemical reaction or metal deposition during the pulse off time and pulse off time voltage is comparatively less than pulse on time voltage. This is why, charged potential (φ_C) can be judged as overpotential *(η)*. From the Butler-Volmer equation, during the pulse on-time, reaction current density *(i)* is:

$$i = i_0 \exp\left(\frac{\alpha n F}{RT} \varphi_C \right) \approx i_0 \exp\left(\frac{\alpha n F}{RT} \varphi_0 \frac{t}{\tau_C} \right) \tag{3}$$

Here, i_0 exchange current density, α leakage factor, F Faraday constant, R gas constant, T temperature, n the number of electrons taking part in the reduction, φ_0 potential. Since the reaction rate is proportional to the reaction current density, i.e. $\zeta(t) \infty i$. This can be represents as

$$\zeta(t) = \frac{i}{nF} = \frac{i_0}{nF}\exp\left(\frac{\alpha F}{RT}\varphi_0\frac{t}{\tau_C}\right) = \frac{i_0}{nF}\exp\left(\frac{\alpha F}{RT\rho c_{DL}}\frac{\varphi_0 t}{d_{gap}}\right) \tag{4}$$

The electrochemical reaction or deposition occurs only during on time of pulse. For this reason the deposition rate can be calculated by integrating the reaction rate during pulse on time. Therefore, localized electrochemical deposition rate, Z:

$$Z\left(\varphi_0, t_{on}, t_{period}, d_{gap}\right) = \frac{1}{t_{period}}\int_0^{t_{on}}\zeta(t)\,dt$$
$$= \frac{d_{gap} f}{\varphi_0}\frac{i_0 RT\rho c_{DL}}{\alpha z F^2}\left[\exp\left(\frac{\alpha F}{RT\rho c_{DL}}\frac{\varphi_0 D}{d_{gap} f}\right) - 1\right] \tag{5}$$

Here, frequency $f = \frac{1}{t_{period}}$ and duty ratio $D = \frac{t_{on}}{t_{on}+t_{off}} = \frac{t_{on}}{t_{period}} = t_{on}\times f \Rightarrow t_{on} = \frac{D}{f}$

(a)

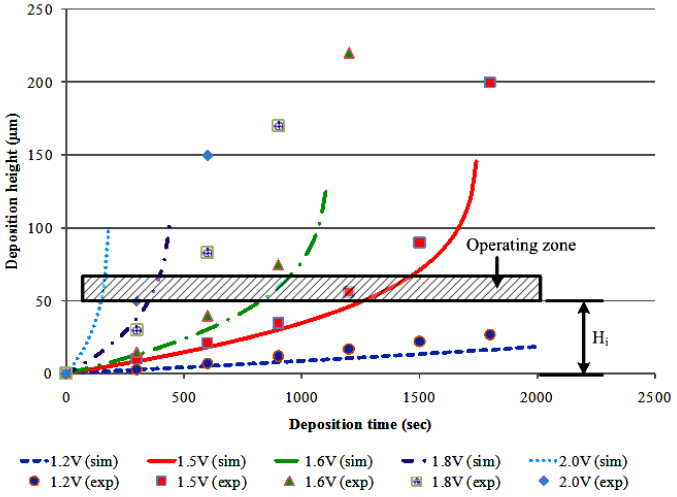

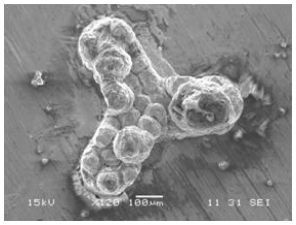

(b)

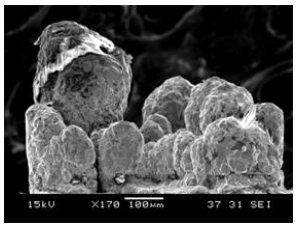

(c)

Fig. 3. (a) Deposition height and Operating zone for LECD process (b) Tree structure of deposited electrode side view (c) top view

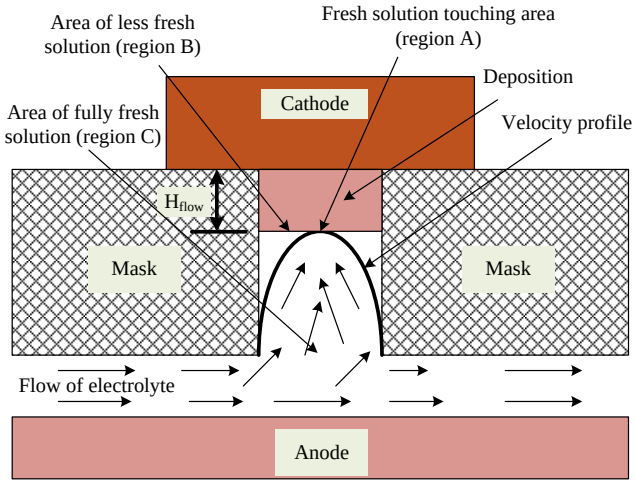

Fig. 4. Concept of FLUENT simulation

Fig. 3 (a) shows the simulation and experimental results of equation (5) where the value of φ_0 is 1.2V, 1.5V, 1.6V, 1.8V and 2.0V. However, the value of f, D and d_{gap} are kept constant on 100 kHz, 0.33 and 350 µm. The simulation and experimental results both indicate that at the beginning of the depositing height the deposition rate is very low, as the deposition height increases the rate is becoming high. This is because, with the increase of deposition height the gap between the anode and cathode will decrease, cause the increase of the deposition rate. Fig. 3 (b) and (c) show the improper

deposited electrode under the condition of φ_0, f, D and d_{gap} are 1.5V, 100 kHz, 0.33 and 350 µm. It can be seen from the fig. 3 that when the deposition height reaches around the mask height (250 µm) the deposition starts become tree type. This is because, after 250 µm there is no mask to guide the deposition structure. For this, in order to increase the aspect ratio of the deposited structure it is needed to lift up the z axis with a close lope control system. If we apply the control algorithm at the beginning of the deposition then it will take long time to reach the desire height, because the deposition rate is very low at the beginning. This is why; the control zone is selected after deposition structure reaches up to certain height. The electrolyte flow region plays a significant role in metal deposition. Depending on the flow pattern, the initial growth height is needed to select. This is why FLUENT analysis is conducted in the mask hole and the gap between anode and mask, in order to fine the actual scenario.

3.2. Determination of limit of the initial growth by FLUENT analysis

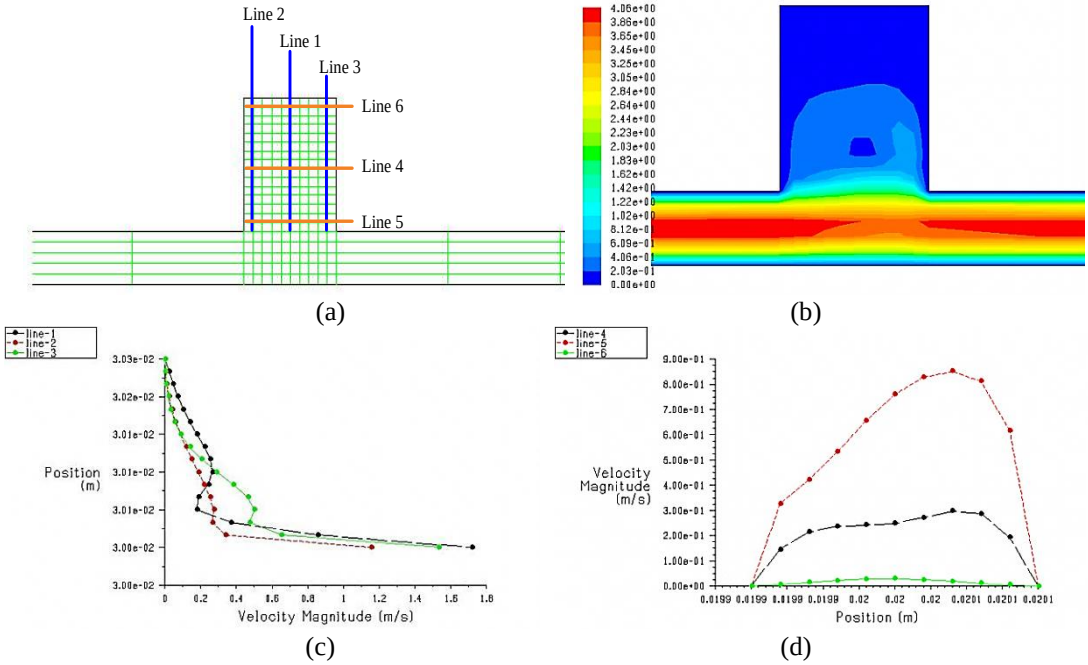

Fig. 5. (a) Grid inside the mask area (b) Flow analysis (c) Velocity for vertical grid line (d) Velocity for the horizontal grid line

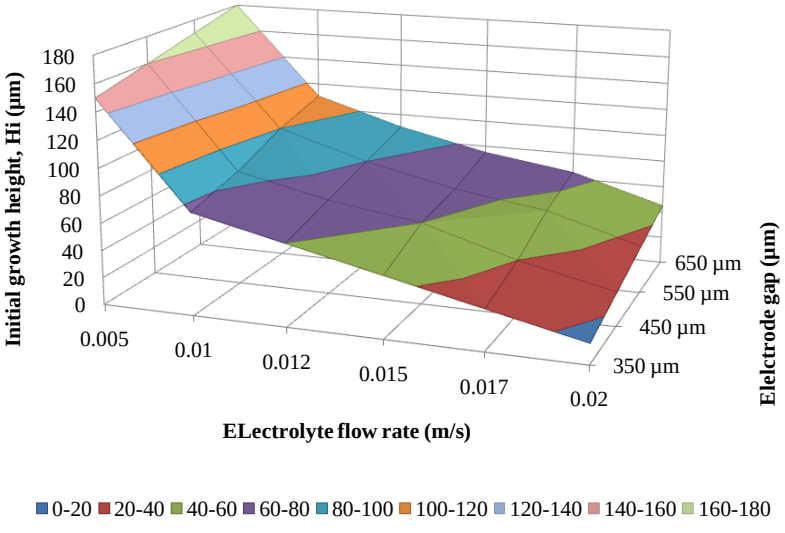

Fig. 6. Surface plot for initial growth height for different flow rate and electrode gap.

It can be seen from Fig. 4, when the electrolyte is flowing through the narrow passage between the mask and the anode, a flow region is created inside the mask. In that flow region, fresh copper ion is always available. Outside the flow region, the

copper ion is reached by diffusion process. If the deposition structure reaches and touches the flow region, then in region A the deposition growth will be higher than the region B. In region B, the fresh copper ion is lesser because ions are reaching there through diffusion and in region A, fresh ions are coming by force convection. If the deposition reaches this zone, then the deposited structure will become tree type. On the other hand, if the deposition reaches up to region C, then there is a chance of become powdery structure. This is why, the initial growth height should not cross the flow region and the initial growth height should be $H_i < H_{flow}$.

Fig. 5 shows the FLUENT simulation for the electrolyte flow 0.01 m/s and 250µm mask height and 100µm gap between the mask and anode. From the above condition, it can be concluded that the safer initial growth height can be 50µm or less than this. For different flow rate condition and different electrode gap, a surface plot was done in Fig. 6. In order to get a high aspect ratio electrode the initial growth height can be selected from the Fig. 6 surface plot. Fig. 7 (a) and (b) show the LECD structure under above operating conditions and using close loop control algorithm within the operating zone. Fig. 7 (c) shows that the micro-EDM hole using the deposited electrode on stainless steel.

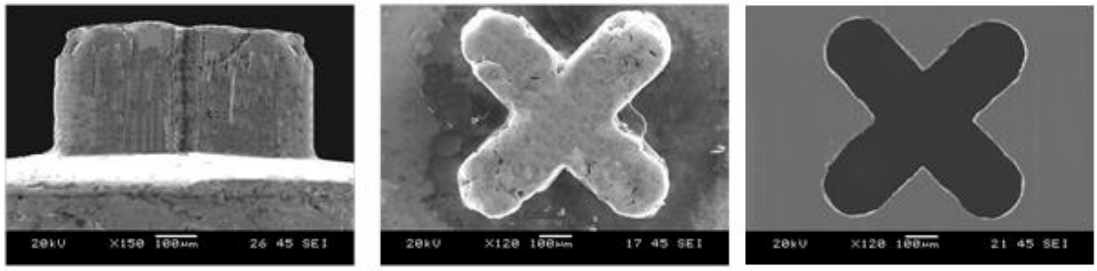

(a) (b) (c)

Fig. 7. LECD electrode (a) side view (b) top view (c) EDM hole on stainless steel using LECD electrode

4. Conclusions

Localized electrochemical deposition is a simple and attractive method for making complex cross sectional electrode. These studies give an idea of the operating parameters range of the electrolyte flow as well as the gap between the anode and mask. By this, it is easy to control the deposition growth. The limiting value is decided from FLUENT analysis, on various electrolyte flow rate and various electrode gap. If the parameters are maintained within these parameters range it is possible to fabricate high aspect ratio micro structure. Finally, the deposited copper electrodes are used as a micro EDM electrode. Micro-holes with good surface quality with rim free of burr-like recast layer are fabricated with the LECD electrode by die-sinking EDM with RC circuit.

References

[1] Habib, M. A., Shaleh, T., Rahman, M., 2010. Modeling for fabrication of micro electrodes by localized electrochemical deposition for micro-EDM. Pro. of the Ins. of Mech Eng, Part B: J. of Engineering Manufacture 224, p.1741.

[2] Hunter, I.W., Lafontaine, S.R., Madden, J.D., 1997. Three-dimensional microfabrication by localized electrochemical deposition and etching, US Patent Specification, 5, 641, 391.

[3] Madden, J.D., Hunter, I.W., 1996. Three-dimensional micro-fabrication by localized electrochemical deposition, J. Microelectromech. System 5, p.24.

[4] Jansson, A., Thornell, G., Johansson, S., 2000. High resolution 3d microstructures made by localized electrodeposition of nickel, J. Electrochem. Soc. 147, p.1810.

[5] El-Giar, E.M., Thomson, D.J., 1997. Localized electrochemical plating of interconnectors for microelectronics, Proc. IEEE Conf. Communications, Power and Computing, WESCANEX, p.327.

[6] El-Giar, E.M., Said, R.A., Bridges, G.E., Thomson, D.J., 2000. Localized electrochemical deposition of copper microstructures, J. Electrochem. Soc. 147, p.586.

[7] Yeo, S.H., Choo, J.H., Yip, K.S., 2000. Localized electrochemical deposition—the growth behaviour of nickel micro-columns, Proc. SPIE 4174, p.30.

[8] Yeo, S.H., Choo, J.H., 2001. Effects of rotor electrode in the fabrication of high aspect ratio microstructures by localized electrochemical deposition, J. of Micromechanics and microengineering 11, p.435.

[9] Yeo, S.H., Choo, J.H., Sim, K.H.A., 2002. On the effects of ultrasonic vibrations on localized electrochemical deposition, J. of Micromechanics and microengineering 12, p.271.

[10] Habib, M. A., Gan, S. W., Rahman M., 2009. Fabrication of Complex Shape Electrodes by Localized Electrochemical Deposition, J. of Materials Processing Technology 209 (2), p.4453.

[11] Habib, M. A., Gan, S. W., Lim H. S., Rahman,M., 2008. Fabrication of EDM Electrodes by Localized Electrochemical Deposition, Int. Journal of Precision Engineering and Manufacturing 9(2), p.75.

Available online at www.sciencedirect.com

SciVerse ScienceDirect

Procedia Engineering 00 (2012) 000–000

Procedia Engineering

www.elsevier.com/locate/procedia

5th BSME International Conference on Thermal Engineering

Tailoring the Molecular Distribution of Bioreactive Chemical Groups to Modulate Adhesion to Soft Tissues

Jahid Ferdous[a], Eva Juarez-Perez[a], Tarek Shazly[a,b,*]

[a]*Biomedical Engineering Program, College of Engineering and Computing, University of South Carolina, Columbia, SC – 29208, USA*
[b]*Department of Mechanical Engineering, College of Engineering and Computing, University of South Carolina, Columbia, SC – 29208, USA*

Abstract

The application of adhesive materials can significantly augment available wound repair techniques and improve healing following surgical interventions. However, soft tissue surface chemistry and mechanical loading conditions significantly vary among potential applications and confound the development of a universal adhesive material with acceptable clinical performance. Current materials are however not designed on a tissue-specific basis and as a result, force a choice between high adhesion strength and biocompatibility. We hypothesize that rational tuning of bioreactive chemical groups distribution along adhesive polymer chains can facilitate optimal tissue-material interactions without inducing a concomitant reduction in material biocompatibility. A series of two-component, aldehyde-mediated adhesive materials are synthesized using dextran aldehyde and chitosan polymers to achieve both cohesive and adhesive cross-linking through the formation of imine bonds. Within the material series, the distribution of bioreactive aldehyde groups along the constituent polymer chains are varied while keeping the total aldehyde content at a constant level. The gelation time, elastic modulus, and adhesion strength to renal artery tissue surfaces are measured for each material formulation. Results show that the reactive chemical groups distribution strongly modulates adhesive interactions. Optimizing material bioreactive groups distribution in a tissue-specific manner could provide a means to circumvent the persistent tradeoff between adhesion and biocompatibility.

Keywords: Adhesive Materials; Adhesion; Biocompatibility; Molecular Distribution; Soft Tissue.

1. Introduction

Soft tissue adhesive materials assist to attain homeostasis, prevent anastomatic leakage, provide mechanical reinforcement to compromised tissue, deliver therapeutic compounds , and thus facilitate tissue healing at surgical sites [1]. Although clinical outcomes of commercially available adhesive materials, such as cyanocrylate and fibrin, are usually satisfactory, they are still limited by biocompatibility and the degree of adhesion, respectively. Highly reactive cyanocrylate strongly adheres with the soft tissue but generates toxic degradation by-products, whereas highly biocompatible fibrin only loosely adheres to tissue surfaces [2-3]. Surface chemistry variation among soft tissues, such as heart, lung, kidney, intestine, and duodenum etc., and diverse mechanical loading conditions, also preclude favorable clinical outcomes in many potential indications for adhesive materials.

Among different strategies to develop effective adhesive materials in recent past, hydrogel-based approaches have attracted more attention due to the potential to tune material properties to optimize material properties, including adhesion strength, degradation kinetics, bulk modulus, and cytocompatibility [4]. Previous studies have shown that aldehyde-

* Corresponding author. Tel.: +1-803-777-4678 ; fax: +1-803-777-0106.
E-mail address: SHAZLY@cec.sc.edu

mediated materials show potential to control adhesive interactions via titration of free aldehyde groups content [5]. Moreover, tissue-specific adhesion has been demonstrated via adjustment of material aldehyde content to match the amine groups available on a targeted tissue surface [6]. Herein we postulate that tissue-material adhesion can be further controlled through tuning of the aldehyde groups distribution along constituent polymer chains – because this can be done at a fixed level of overall aldehyde groups content, the proposed strategy is anticipated to maintain material biocompatibility.

In this study, a family of adhesive materials having four different aldehyde groups distributions is synthesized and characterized. The total number of aldehyde groups was kept constant among formulations to ensure that property variations were not a consequence of net material reactivity, but rather due to the presentation of reactive groups along polymer chains. Results indicate the gel formation time does not change significantly until the spacing between two aldehyde groups reaches the threshold value. Moreover, a stiffer material is formed when distance among aldehyde groups is small. Tissue-material adhesive interactions with porcine renal arteries reveal that adhesive strength is also modulated by the aldehyde groups distribution, although in a complex manner that warrants further investigation. Our results provide preliminary indication that rationale tuning of the bioreactive chemical groups distribution can provide a basis for optimization of tissue-specific adhesive materials.

2. Materials and methods

2.1. Material synthesis

A series of two-component, aldehyde-mediated adhesive materials were synthesized using dextran aldehyde and chitosan polymers. A 10 wt.% aqueous solution of dextran with an average molecular weight of 40 kDa was mixed with a 5-15 wt.% solution of sodium periodate at room temperature to yield dextran aldehyde with different oxidation levels, herein defined as the percent of oxidized glucose rings measured via acid-base titration (Fig 1a). The solution was then dialyzed, lyophilized, and reconstituted to yield an aqueous polymer solution of dextran aldehyde. A 2 wt% aqueous solution of chitosan with an average molecular weight of 340 kDa was also prepared, providing a cohesive material component whose amine groups can chemically cross-link with dextran aldehyde through imine bond formation. Material components (dextran aldehyde and chitosan) were loaded into and delivered with a dual-chamber syringe equipped with a 12-step mixing tip, enabling repeatable component mixing and material network formation (Figure 2a). The average distance between rings containing aldehyde groups in terms of the monomer repeating unit is defined as the distribution index, and systematically varies among material formulations. A constant number of aldehyde groups and ratio between aldehyde to amine groups were maintained through adjusting the dextran aldehyde solid content prior to material formation (Table 1).

2.2. Gelation time

Constant volumes of dextran aldehyde and chitosan solutions were injected using dual-chamber syringe into a 24 well culture plate where a magnetic stir rod was rotating at a predefined fixed speed. The time to form a solid globule around the magnetic stir rod by visual inspection was considered as the gelation time. Results are presented as the average and standard deviations of three independent readings for each material compositions.

Table 1. Composition descriptions of the investigated dextran aldehyde:chitosan material series

Composition	Dextran Aldehyde					Chitosan			Dextran aldehyde:Chitosan
	Molecular Weight (kDa)	Percent Oxidation (%)	Solid Content (%)	Distribution Index	Aldehyde Content (# per ml)	Molecular Weight (kDa)	Solid Content (%)	Amine Content (# per ml)	Reactive Groups Ratio ($CHO:NH_2$)
A	40	19.44	13.25	5.14	2.30×10^{20}	340	2	7.63×10^{19}	3
B	40	24.30	10.80	4.11	2.30×10^{20}	340	2	7.63×10^{19}	3
C	40	42.12	6.30	2.37	2.30×10^{20}	340	2	7.63×10^{19}	3
D	40	71.28	3.59	1.40	2.30×10^{20}	340	2	7.63×10^{19}	3

2.3. Compressive elastic modulus (E_c)

Cylindrical samples of the materials were prepared using silicon mold with a diameter and height of 9.5 mm and 6.25 mm, respectively, and subsequently used to measure the compressive elastic modulus (E_c). Uniaxial tensile testing (Bose® Biodynamic Test Instrument, Minnetonka, MN) was used to apply ramped uniaxial compressive displacement (maximum 30% of initial samples' height with a rate of 0.005 mm/sec). Sample forces and displacements data were continuously recorded at a data acquisition rate of 1.67 points/sec using a software package (Wintest® Software, Minnetonka, MN). Force and displacement data were transformed into true stress and strain for each material composition to calculate E_c. Results are presented as the average and standard deviations of three independent readings for each material compositions.

2.4. Adhesion strength

Fresh intact porcine kidneys were collected from local slaughter house and stored in the normal saline at low temperature before dissection. Renal arteries were carefully separated from the kidneys and attached with the connectors of uniaxial tensile testing (Bose® Biodynamic Test Instrument, Minnetonka, MN) using parafilm in such a way that the adventitia layer were placed outside and formed a flat surface (Fig 3b). A controlled volume of adhesive material was injected into one tissue surface followed by immediate attachment with the other surface under specified initial compressive load. A constant curing time was maintained for all the samples prior to mechanical testing. Ramped uniaxial tensile displacement (maximum 5 mm with rate of 0.005 mm/sec) was applied and corresponding force and displacements data were recorded using a software package (Wintest® Software, Minnetonka, MN). The maximum load prior to tissue-material interfacial failure was recorded and reported as the maximum adhesion strength. Results are presented as the average and standard deviations of four independent readings for each material compositions.

3. Results and discussion

Dextran aldehyde oxidation level is directly dependent on the amount of oxidizing agent (sodium periodate) (Fig 1b). Prolonged mixing between dextran and sodium periodate ensures the conversion of dextran into dextran aldehyde with no intermediate products. More than 50% glucose chains of 40 kDa dextran open and proportionally the number of reactive aldehyde groups increase when 15 wt% sodium periodate was used in comparison to 5 wt%. The molecular weight of the oxidized polymer is a function of the level of oxidation. Moreover, for a fixed amount of sodium periodate, the initial dextran molecular weight controls the level of oxidation (data not shown).

Alternation in aldehyde groups distribution results in similar gel formation time among materials except for in case A, which has maximum solid content with minimum oxidation level (Fig 2b). The gelation time can be easily lowered by increasing the solid content to achieve a gelation time more suitable for surgical applications. In general, higher solid content and percent oxidation promote network formation through increasing the possibility of cohesive chemical interactions with chitosan amine groups [7]. However, case A having the maximum aldehyde groups distribution index results in almost 3-fold higher gelation time compared to the other formulations. This suggests that a critical aldehyde groups distribution index may exist (between 5.14 and 4.11) above which material cross-linking is depressed due to steric inhibition, as further supported by the observed reduction in material stiffness at higher distribution indices (Fig 2c). Insignificant elastic modulus change is observed when the aldehyde groups distribution index is below 2.37.

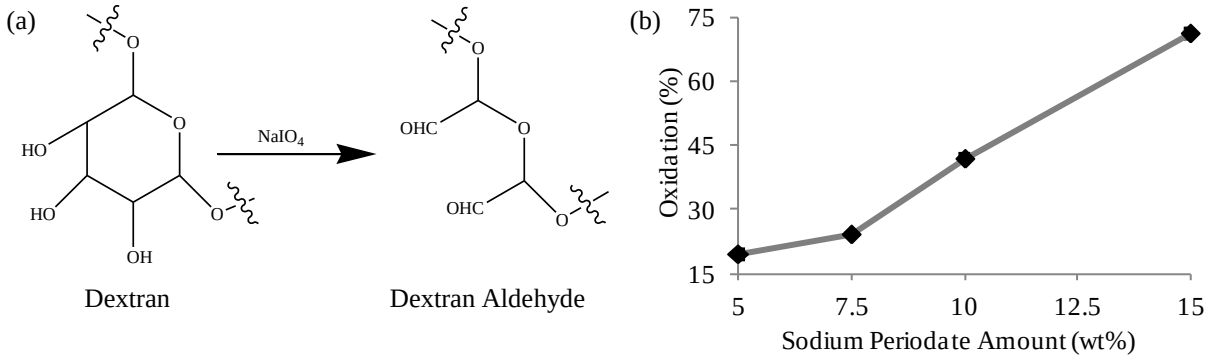

Fig. 1. (a) Sodium periodate oxidizes the dextran glucose ring and results two aldehyde groups; (b) Higher amount of sodium periodate opens more glucose rings and increases the oxidation level of dextran aldehyde.

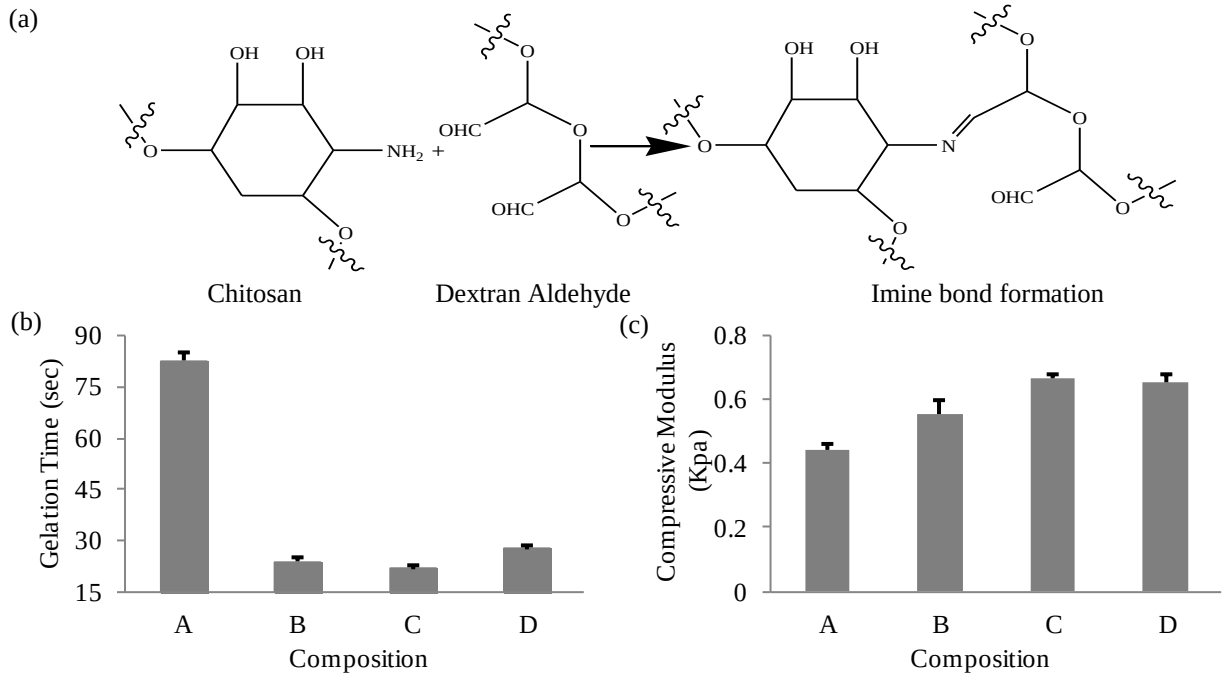

Fig. 2. (a) Imine bond formation between chitosan and dextran aldehyde; (b) Aldehyde groups distribution index affects the gelation time only when it is above the critical value; (c) Material stiffness increases when average distance between two open glucose rings decreases.

The adhesive strength of the material to the tissue surface depends on imine bond between the aldehyde groups of the dextran aldehyde and amine groups of tissue-present proteins (Fig 3a), similar in principle to the formation of internal material cross-linking (Fig 2a). When tissue-material constructs are placed in tension, all formulations underwent cohesive failure indicating that tissue-material cross-linking exceeds internal network formation. Adhesive variation with distribution index indicates that intermediate spacing diminishes adhesive strength compare to distributions at the ends of the examined range. This non-monotonic response suggests the existence of multiple reactive groups distributions that promote efficient tissue-material interactions, and motivates further examination of this approach to optimize tissue-specific adhesion.

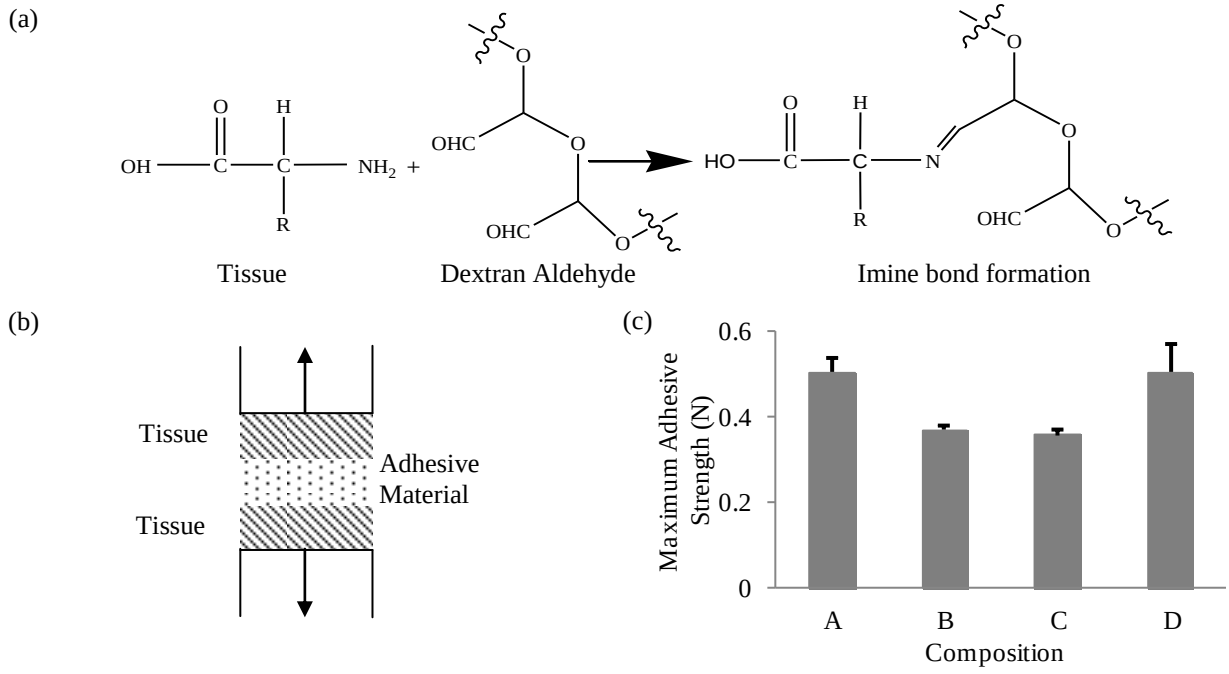

Fig. 3. (a) Imine bond formation between tissue and dextran aldehyde; (b) Schematic of tissue-material interface for adhesive strength measurement; (c) Aldehyde groups distribution index alters tissue-material adhesive strength.

Variation in reactive chemical groups distributions is hypothesized to differentially affect adhesion to other tissue types, as they exhibit different surface amine distributions for adhesive bond formation. Moreover, subsequent studies of the effects of aldehyde groups distribution index on biocompatibility, swelling and erosion kinetics, and adhesive interfacial morphology are required to fully explore the proposed method of optimizing tissue-specific adhesive materials.

Acknowledgements

This work was supported by the National Science Foundation/EPSCoR Grant (EPS-0903795).

References

[1] Jackson, M. R., 1996. Tissue sealants: Current status, future potential, Nature Medicine 2(6), p. 37.
[2] Tseng, Y. C., Tabata, T., Hyon S. H., Ikada, Y. 1990. *In vitro* toxicity test of 2-cyanoacrylate polymers by cell culture method. Journal of Biomedical Materials Research 24, p. 1355.
[3] Silver, F. H., Wang, M. C., Pins, G.D., 1995. Preparation and use of fibrin glue in surgery, Biomaterials 16(12), p. 891.
[4] Peppas, N. A., Sahlin, J. J., 1996, Hydrogels as mucoadhesive and bioadhesive materials: A review, Biomaterials 17, p. 1553.
[5] Shazly, T. M., Artzi, N., Boehning, F., Edelman, E. R., 2008. Viscoelastic adhesive mechanics of aldehyde-mediated soft tissue sealants, Biomaterials 29, p. 4584.
[6] Artzi, N., Shazly, T., Baker, A. B., Bon, A., Edelman, E. R., 2009. Aldehyde-Amine chemistry enables modulated biosealants with tissue-specific adhesion, Advanced Materials 2(6), p. 637.
[7] Artzi, N., Shazly, T., Crespo, C., Ramos, A. B., Chenault, H. K., Edelman, E. R., 2009. Characterization of star adhesive sealants based on PEG/Dextran hydrogels, Macromolecular Bioscience 9(8), p. 754.

Available online at www.sciencedirect.com

SciVerse ScienceDirect

Procedia Engineering 00 (2012) 000–000

Procedia Engineering

www.elsevier.com/locate/procedia

5th BSME International Conference on Thermal Engineering

Effect of grog amounts and sizes on the properties of fireclay bricks

N. Halder[a], A. Hushna[a]*, R. Haque[a]

[a]*Department of Materials and Metallurgical Engineering, Bangladesh University of Engineering and Technology (BUET), Dhaka—1000, Bangladesh*

Abstract

This paper reports the feasibility of the production of fireclay bricks from locally available fireclay and grog that can provide reduced shrinkage of the finished product and negligible shape change at high temperature operations. The fireclay refractory bricks are usually manufactured using clay as raw material. But the addition of the grog (refractory particles obtained from fired solid refractory bricks) into the clay can be a very effective method of producing better quality fireclay bricks. The incorporation of these grogs in varying sizes and contents can provide upgrading of the physical, mechanical and thermal properties of plain fireclay brick to a greater extent. For this, the chemical analysis of fireclay was carried out. Then fireclay bricks of size 77.5mm x 38.4mm x 26mm with different grog sizes (2.38 mm-1.68 mm, 1.68 mm-595 micron, 595-250 micron) and amounts (10%, 20%, 30%, 40%, 50%) were prepared using stiff-mud process and uniaxial pressing. After drying and firing, properties like-drying and firing shrinkage, apparent density, porosity, cold crushing strength and spalling resistance were measured. Comparing these values, the most suitable grog-incorporated fireclay brick with the best combination of those properties which can serve the purposes better was found out. The best combination of physical, mechanical and thermal properties in this work has been obtained from the brick specimen made of 20-30% grog content.

Keywords: Grog, firebricks, firing shrinkage.

1. Introduction

Fireclays are hydrated aluminium silicates represented by $Al_2O_3.2SiO_2.2H_2O$. At higher temperature water is driven out. In nature it is usually found to contain 24-45% Al_2O_3, 50-80% SiO_2 and loss on ignition (LOI) between 9 -12%. A good fireclay should have 24-26% plasticity and shrinkage after firing should be within 6-8% maximum. It should also contain less amount of Fe_2O_3 [1].Fireclay is generally of sedimentary origin. Impurities like oxides of calcium, iron, titanium and magnesium and alkalies are invariably present [1]. The term 'firebricks' refers to fireclay bricks. It is classified in several kinds of clays e.g. flint, plastic clay, kaolin, etc. Fusion temperature of fireclay (varies between 1580 to 1750^0C) is lowered by the presence of alkalies, sand, gravel, calcium silicate, iron oxide, magnesium silicate, iron silicate etc [2].

Grog is fireclay which has already been heated to, say, 1300^0C so that no further contraction in volume takes place. Broken and used fireclay bricks can be used as grog. A small amount of plastic clay is added to facilitate moulding. A mixture is made by grinding raw fireclay, grog and plastic clay with water. Grog addition to fireclay is mainly as an anti-shrinkage element in the form of angular particles of various sizes to achieve better interlocking of grains [2]. Grog acts as skeleton to hold the brick together in a stable form during firing operation [3]. As the grog particles are stable in size, the overall drying and firing shrinkage is reduced. Grog addition ranges from 20 to 90% in the clay mixture depending upon the properties of raw clays and the desired properties of finished product [2].

A useful property for refractories is apparent and true density. The true and apparent density depends on the density of the

* Corresponding author. Tel.: +88-01717702452;
E-mail address: mithi831@yahoo.com

constituents in the raw materials and the final products, the moulding pressure, the degree of sintering and amount of porosity. The more dense the raw materials, the higher the true and apparent density of the end products. True and apparent density increases with the increase in moulding pressure and the degree of sintering whereas the density decreases with increasing porosity.

Porosity is a measure of void space in a material. The porosity depends on the constituents in the raw material and the final products, the moulding pressure, the degree of sintering and the true and apparent density.

The cold crushing (CCS) of fired refractory is not of high importance but it serves as a guide other characteristics such as vitrification, burning temperature and purity of material.

Porous course grained refractories have poor crushing strength whereas dense and fine grained refractories generally have good crushing strength [2].

Spalling is defined as the fracture of the refractory brick or block due to a temperature gradient in the brick for uneven heating or cooling that sets up stresses causing failure. Resistance to spalling can be increased by using a coarse grog, by increasing the porosity, by decreasing the coefficient of expansion, by increasing strength of brick and by increasing thermal diffusivity [2].

2. Experimental procedure

2.1 Raw materials and production of bricks

The sequence of operations were followed in the following three stages –processing of raw materials, preparation of specimen, measurement of properties. The processing of raw materials included selecting the suitable types of raw materials to be used for preparing the specimens, primary processing of these materials to make them suitable for next operation and determining the chemical compositions. Three types of raw materials were used here-clay, grog and water. The clay used here was fireclay, collected from the local market. The fireclay particles were very fine, naturally dried and granular in shape. It was sieved to avoid any unwanted foreign particles like- stone particles, large aggregates or other substances and to get homogenous fine clay.

The determination of the components of the fireclay was performed but the chemical analyses of the grog particles were not done. The determination of percentage of SiO_2, Fe_2O_3 and Al_2O_3 of the given fireclay was done. The chemical analysis of the fireclay is given in table 1.

Table 1: Chemical analysis of the fireclay

Constituents	Weight Percentage
SiO_2	66.29%,
Al_2O_3	20.59%,
Fe_2O_3	4.55%.

The source of grogs was the fired solid and porous refractory bricks collected from thelocal market. These large solid bricks were first crushed and then broken into desired small sizes by hammering. The shape of the grog particles was granular and porous. The grogs were then separated into three specific sizes by sieving through corresponding numbered sieves using Taylor's sieve analyzer method. Three sizes of grog were taken- (a) +2.38mm -1.68mm, (b) +1.68mm-600micron, (c) +600micron- 250 micron and grog percentages were-10%, 20%, 30%, 40, 50%. Water was mainly used as a binder. After drying, the water is completely removed from the specimens. According to the percentage of the clay and the grogs, almost 10% water was used for preparing every specimen.

Preparation of specimen involved mixing, moulding, drying and firing. Fireclay, water, crushed and sieved grog were first proportioned and then mixed through stiff-mud process. Hand-moulded bricks were prepared using uni-axial pressing. Green bricks were then subjected to air and sun drying for 5-6 days each and to oven drying for 6 hours at 120^0C. Firing was then done in the muffle furnace at 1000^0C for 6 hours and fired bricks were obtained after furnace cooling [4].

The manufacturing process of brick specimen is given in short in the Figure 1-

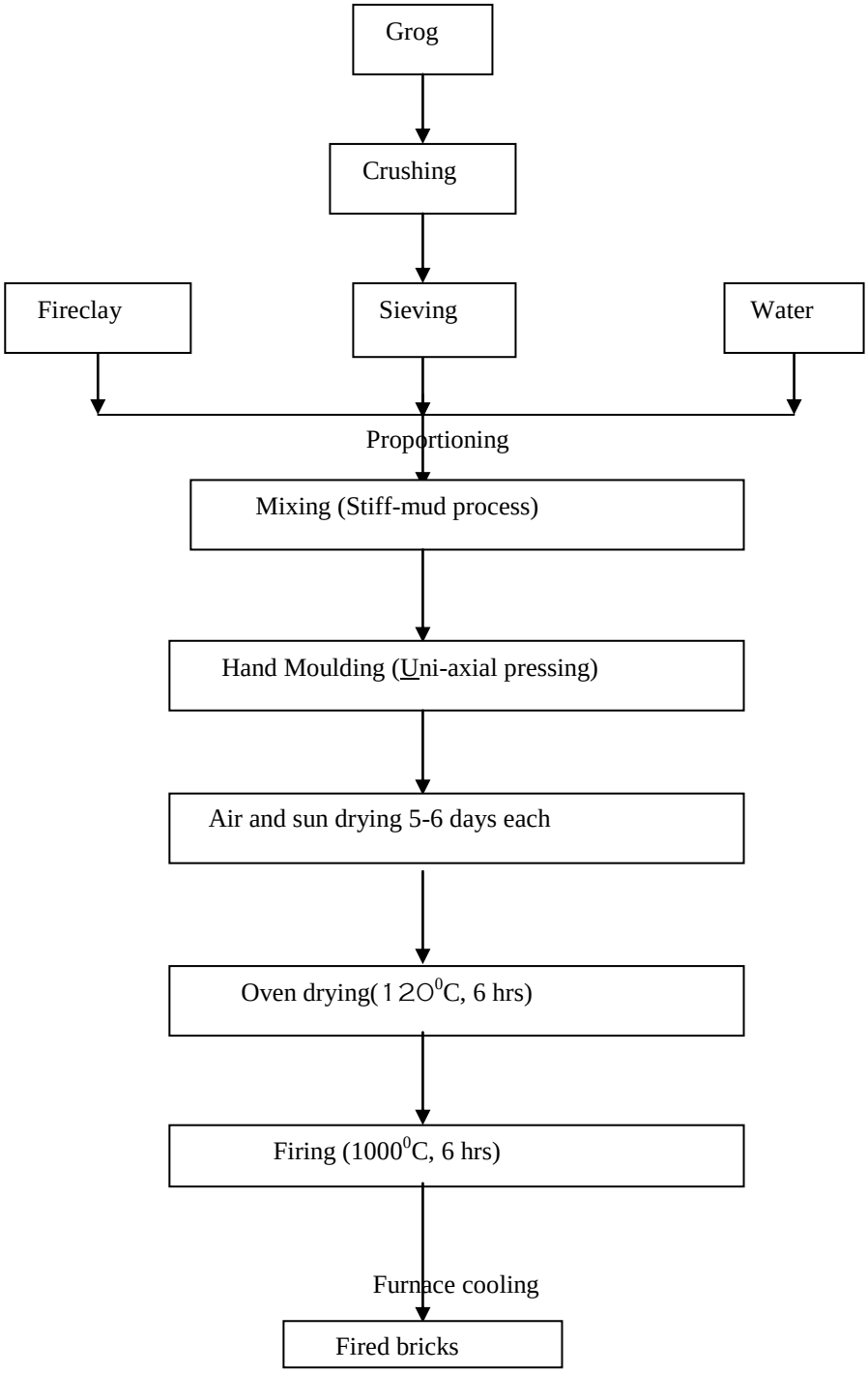

Fig. 1: Flow sheet Diagram for Fireclay brick manufacturing

The total types of specimens are given in table 2.

Table 2: Types of specimens prepared with different amount of grogs

Grog size (micron)	Grog content (wt%)	Clay content (wt%)	H_2O content (wt%)	No. of bricks	Avg. brick dimensions (mm)
+2680,-1380	0	100	~10%	3	Length: 77.5
	10	90			
+1380,-595	20	80			Width: 38.4
	30	70			
+595,-250	40	60			Thickness: 26
	50	50			

2.2 Measurement of properties

Among the properties of the fired specimens, the drying and firing shrinkage, the apparent and true densities, total porosities in percentage, the cold crushing strength and spalling resistance were measured and compared. The measuring procedures are described below-

Measurement of drying and firing Shrinkage: The volume of the block before drying, after drying and after firing was measured. Drying shrinkage and firing shrinkage were then measured from these volumes.

Measurement of apparent/true density and porosity: Apparent density was measured after measuring weight and volume. True density was measured after crushing the block and using the pycnometer bottle. From apparent density and true density, total volume of pore is estimated.

Measurement of cold crushing strength: A standard mechanical or hydraulic compression machine is used. The specimen is placed in between two rams which move when the machine is switched on. The load is applied to the surface of the specimen. The cold crushing strength of the specimen is measured from the total maximum load and average of the gross area.

Measurement of spalling resistance: The refractory block is weighed. Then it is placed in a muffle furnace at a temperature of about 850-9000C, held for 15 minutes, removed and cooled under circulating air for 5 minutes and again replaced in the furnace for reheating. This cycle is repeated for 5 times then the block is weighed. Spalling resistance was measured from the difference between these two weights.

3. Results and discussion

3.1 Drying Shrinkage

The effects of grog sizes and amounts on drying shrinkage are shown in the Fig. 2.

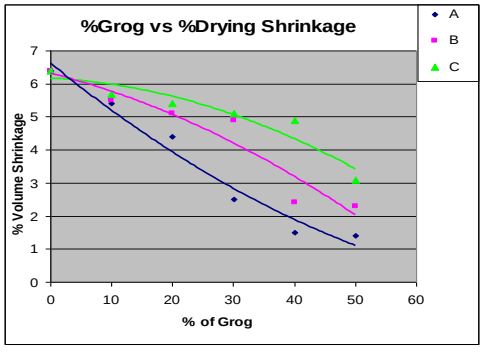

Fig. 2: Effect of Grog on Drying Shrinkage

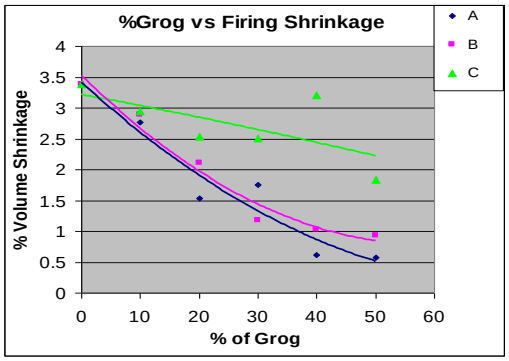

Fig. 3: Effect of Grog on Firing Shrinkage

From the figure we see that for 100% clay the drying shrinkage was maximum, 6.4%. The drying shrinkage decreases with increasing percentage of grog from 0% to 50%.The drying shrinkage also decreases with increasing size of grog from C (smallest) to A(largest). The possible reasons behind this are given below.

With increasing plastic part or clay, the amount of water absorption increases during mixing. This water remains between the clay particles and while drying this water evaporates and that is why shrinkage of bricks occurs. More the amount of clay more will be the shrinkage. Grog absorbs less water than clay and as grog has a stable mass they do not shrink during drying. That may be the reason of decreasing drying shrinkage with increasing grog amount.

3.2 Firing Shrinkage

The effects of grog sizes and amounts on firing shrinkage are shown in the Fig. 3. From the figure we see that for 100% clay the firing shrinkage was maximum (3.38%). The firing shrinkage decreases with increasing percentage of grog from 0% to 50%.The firing shrinkage also decreases with increasing size of grog from C (smallest) to A(largest). The possible reasons behind this can be that- when the clay is fired decomposition of clay occurs and combustible, volatile matter and any molecular water present is driven out and at higher temperature of firing fusion of various components of clay occur. All these cause shrinkage of clay during firing. But the grog that is used with clay has already been fired earlier and has reached a stable volume and the grog also does not get fused during firing. So they act as skeleton to hold the brick together in a stable form during the firing operation. As grog do not shrink during firing so with increasing grog percentage firing shrinkage decreases.

3.3 Apparent density and porosity

The effects of grog sizes and amounts on density are shown in the Fig. 4 and the effects of grog sizes and amounts on porosity are shown on the Fig. 5.

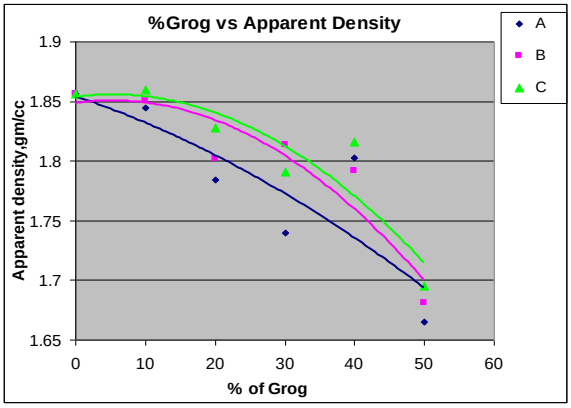

Fig. 4: Effect of Grog on Apparent Density

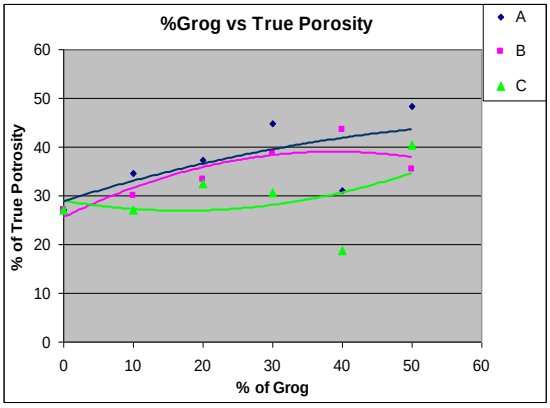

Fig. 5: Effect of Grog on True Porosity

With increase in the percentage of the grogs, the percentage of total porosity gradually increase and the apparent density gradually decrease. The possible reasons behind that are given below-

Grogs are the porous and non-plastic parts of the brick and thereby do not shrink on firing. Instead, the particles tend to resist the shrinking[5]. Only clay particles, being plastic shrink on firing which gives the overall shrinkage. So an increase in the percentage of grog means more resistance to shrinking which will result in reduced shrinkage. And a reduction in shrinkage means more presence of voids within the specimen which gives porosity in increasing proportion.

Again, an increase in porosity means decrease in mass due to more void space in the specimen and less shrinkage mean less change in apparent volume, which in turn gives a reduced apparent density. Thus, with increase in percentage of the grog amount, the percentage of total porosity increase and the apparent density decrease.

With decrease in the size of the grog, the percentage of total porosity gradually decrease and the apparent density gradually increase. As the fineness of the particles increases, the mixing and bonding become more uniform, and during pressing, the particles are more compacted giving reduced amount of void space and thereby reduced apparent volume. So the porosity decrease and the apparent density increase with decrease in the grog size[6].

The specimen with 100% clay shows minimum porosity and maximum apparent density. As there is no grog to resist the shrinkage, so 100% clay shows the maximum amount of shrinkage thereby giving minimum amount of porosity and a maximum apparent density.

3.4 Cold crushing strength

The effects of grog sizes and amounts on cold crushing strength are shown in the Fig. 6. Irrespective of the size of the grogs, the cold crushing strength of the specimens is maximum for 100% clay or 0%grog. With increase in grog content, the cold crushing strength shows a decreasing order.

On firing, the non-plastic grog materials being once fired do not show any type of fusion or bonding. The clay particles, having enough plasticity, are fused and give a fused mass of Al2O3.SiO2 which provides strong bonding after firing. So more the amount of clay, stronger the bonding and the higher is the load value required to crush it giving higher cold crushing strength. That is why the specimen with 100% clay gives the

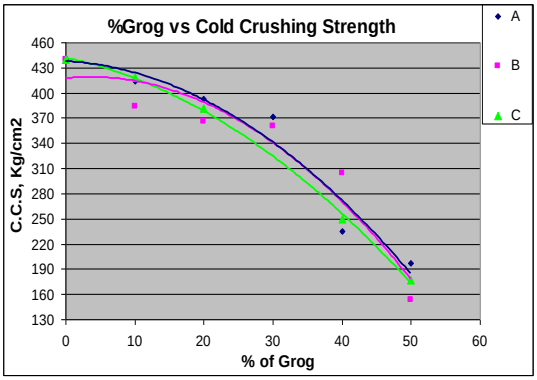

Fig. 6: Effect of Grog on Cold Crushing Strength

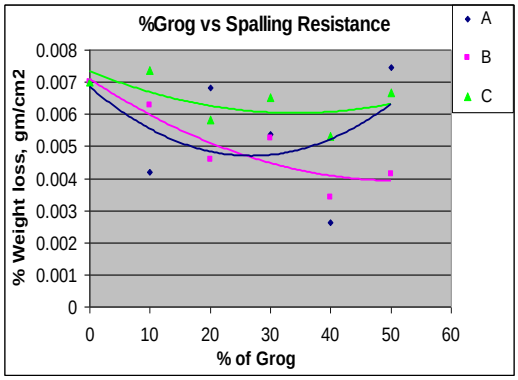

Fig. 7: Effect of Grog on Spalling Resistance

maximum value of strength. Upto 20-30 % grog, decrease in cold crushing strengths were gradual but after that cold crushing strength decreases very rapidly with increasing grog amount.

Now the increase in the grog amount means the decrease in the clay amount proportionately which will give in turn less amount of plasticity and thereby comparatively weaker bonding [7]. So they will be crushed at lower load values giving lower cold crushing strength.

The change in cold crushing strength with grog size was very negligible, that is why the effect of grog size on the cold crushing strength was not studied.

3.5 Spalling resistance

The effects of grog sizes and amounts on spalling resistance are shown in the Fig. 7. The weight loss percentage is in the order of 10-3. That means the weight loss of the brick is very less at the experiment temperature. Maximum %weight loss is for 100% clay or 0% grog. So, 100% clay has the lowest spalling resistance. With increasing percentage of grog spalling resistance increases (%Weight loss decreases) from 0% to 50% grog for the size B and C. For the grog size A, spalling resistance at first increases (%weight loss decreases) with increasing grog upto 25% and then decreases with increasing grog upto 50%.

During the experiment of spalling resistance, weight losses occur due to the combination of thermal fluctuation and mechanical loss during handling (such as, charging and discharging). We assume that mechanical loss is same for all bricks. But in case of the largest grog size, A, with increasing percentage of grog, void increases and thus the grog may be loosely bonded for higher percentage of grog. This loosely bonded grog can fall off during handling more easily from the surface and thus mechanical weight loss or total weight loss may increases with higher percentage of grog for the size A.

4. Conclusion

The following conclusions may be drawn from the work done so far:

- The drying shrinkage decreases with increasing amount and size of grog
- The firing shrinkage decreases with increase in grog percentages and grog size.
- The total porosity of the fired specimens increase with increase in both the grog percentage and its size.
- The apparent density of the fired specimens decreases with increase in both grog percentage and its size.

- The cold crushing strength of the fired specimens decreases with increase in the grog percentage irrespective of its sizes.
- The spalling resistance increases with increasing grog percentage and size. But for the largest grog at first spalling resistance increases and then decreases.

The best combination of physical, mechanical and thermal properties in this work has been obtained from the brick specimen made of 20-30% grog content. From studying the properties of brick we see that, at these compositions the cold crushing strength of bricks is high enough (360-392 kg/cm2) for furnace operation and also the other properties, such as porosity, density, spalling resistance, drying and firing shrinkage are quite reasonable.

Acknowledgements

The authors acknowledge the Materials and Metallurgical (MME) Department of BUET for experimental support.

References:

[1] http://www.mineralszone.com/minerals/fireclay.html

[2] O.P Gupta, 1998, Elements of Fuels, Furnaces, & Refractories, pg 665, 674, 675, 679, 681, 742, 743, 744, 748,751.

[3] Norton, “Refractories”, pg125,126,127,136,137,182,183,263.

[4] Mahmud Alam , Effect of grog on the properties of fireclay refractory , B.Sc Engineering Thesis, Dept of MME, BUET, January 2008.

[5] C. M. F. Vieira, S. N. Monteiro, Recycling of grog by addition into red ceramics, Congreso conamet/Sam 2004.

[6] http://www.studiopotter.org/articles/back_1#Vol4No2

[7] http://en.wikipedia.org/wiki/Refractory

Available online at www.sciencedirect.com

SciVerse ScienceDirect

Procedia Engineering 00 (2012) 000–000

Procedia Engineering

www.elsevier.com/locate/procedia

5th BSME International Conference on Thermal Engineering

Development of biomass stove for heating up die barrel of rice husk briquette machine

Md. Ahiduzzaman[a,*], A.K.M. Sadrul Islam[b]

[a]*Bangabandhu Sheikh Mujibur Rahman Agricultural University, Gazipur-1706, Bangladesh*
[b]*Islamic University of Technology, Board Bazar, Gazipur-1704, Bangladesh*

Abstract

In rice husk briquette production process, electricity is used to drive the screw press and to heat up the die barrel. In the energy-starve countries, electricity consumption for producing biomass briquette fuel is not rationale. To reduce the electricity consumption in biomass briquette production process, a biomass fired stove is developed to use as the replacement of the electric heater. The biomass stove is capable of raising the temperature of die barrel at desired level for making briquette. The stove is made of refractory brick and clay. The stove is fired with rice husk briquette. The stove provides heat to die barrel instead of electric heater. The stove shows satisfactory performance by replacing the 6 kW electric-heater in this study. The modified rice husk briquetting machine consumed about 76 kg of rice husk briquette and about 80 kWh of electricity to produce one tonne of rice husk briquette instead of 179 kWh of electricity consumption by traditional rice husk briquetting machine for same quantity of rice husk briquette produced. Hence at least 50% of electricity consumption for rice husk briquette production could be replaced by using the modified technology discussed in this paper.

Keywords: Rice husk briquette, Electricity, Biomass stove, Electric heater, CO_2 reduction cost

Nomenclature

MJ	mega joule
kg	kilogram
kWh	kilo-watt-hour
CO_2	carbon dioxide
h	hour
kW	kilo-watt
rpm	revolution per minute
BDT	Bangladeshi Taka
NPV	net present value

1. Introduction

Biomass densification is not a new technology in the world, though it appeared in Bangladesh in 1990. By densification process loose, low bulk density biomass is compacted into high bulk density materials. Different types of densification methods are commercially available namely, pelleting, cubing, rolling-compressing and briquetting. Rice husk densification technology known as briquetting was introduced in Bangladesh around 1990 by a private entrepreneur. An entrepreneur in Sylhet district (eastern part of the country) imported a briquette machine from Taiwan and set up a factory. Later the technology was adopted into few other places namely, Khulna, Chittagong, Rangnpur and so on. The most widely used densification process in the developing countries is screw extrusion process, known as heated die screw press briquetting. For making biomass briquette fuel, extrusion process called heated die screw press briquetting is used and rice husk is used as raw material for briquetting in Bangladesh [1-2]. Compaction ratio ranges from 2.5: 1 to 8.25:1 or even more [1, 3-4].

This densified biomass fuel is dry woody material and its calorific value ranges from 14.2 to 17.5 MJ/kg, and it is equivalent to "B" grade coal in terms of calorific value. It burns slowly with less smoke than wood fuel [1]. The development of biomass densification technology in Bangladesh has proceeded with own interests and efforts of individual owners and manufacturers [5].

2. Justification of the study

The husk briquette is very much popular fuel alternative to wood fuel. The briquette producing machine is screw extruder type. During the study it is observed that electricity is consumed to produce the briquette from rice husk. Main components of the electricity consumption are the motor and the electric heater. The heater capacity ranges from 6 to 9 kW. The motor capacity of the machine is found to be around 15 kW. The production capacity of the briquette machine is estimated to be 80 to 100 kg/h. Amount of electricity consumption is estimated to be around 200 to 250 kWh to produce each tonne of briquette [7-8]. Whereas in laboratory research, it was found that average energy consumption was 116 kWh/tonne [2]. Bhattacharya et al. [9] reported that the consumption of electricity for briquette production is 179 kWh/tonne. But the electricity is very scarce in Bangladesh. As energy starve country electricity consumption for producing biomass briquette fuel is not fair. One effort was found to replace the electric heater with steel made briquette fuel fired stove for die heating. The fuel consumption of the stove was 4.5 kg/h instead of 6-kW electrical heater. It could save 35 % of total electrical energy consumption [9]. Also local producer tried to use kerosene stove instead of electric heater. All these efforts have been made to reduce electricity consumption for producing husk briquette. Operational cost of kerosene stove is comparatively higher and also the heat distribution is not uniform round the die of briquette. Steel made briquette stove also costly and need special skill to fabricate. To overcome the above barriers a new concept has been developed for die stove made of refractory brick and clay. The advantages of this stove would be the uniform distribution of heat due to the higher content of heat in refractory material and also the clay-brick work is very much simple and can be fabricated easily.

2. 3. Description of the screw extrusion process

In the screw extrusion process, rotating screw conveys the material from the feed port through the die barrel, and compact it in the die (Fig 1. and Fig 2.).
Biomass is forced into intimate and substantially sliding contact with the barrel walls in this process. The combined effects of the friction caused at the barrel wall, the heat from die heater and high rotational speed (~600 rpm) of the screw cause an increase in temperature in the closed system which helps in heating the biomass. Then the biomass is forced through the extrusion die, where the briquette with the required shape is formed [6].

Generally the temperature is maintained between 250°C to 300°C during the briquetting process. Thermal decomposition of raw material begins when it gets heated to about 220°C and the lignin of the biomass material becomes relatively soft. Due to the softening of the lignin the area of inter-particle contact is increased and they form local bridges. The soft lignin works as the binding material, therefore no additional binder is required. The moisture gets evaporated and helps in moistening the biomass. The biomass is compressed further in the die barrel (about 280°C) to form the final product briquette [1, 6].

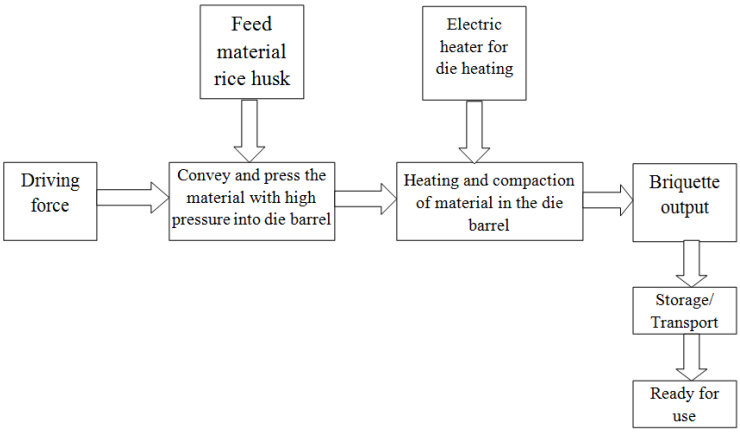

Figure 1. Block diagram of screw extrusion biomass densification process

(a) Photographic view of extruder

(b) Screw of the extruder

(c) Electric heater surround the die

Figure 2. Photographic of (a) rice husk briquette machine, (b) screw and (c) electric heater

4. Materials and Methods

Detail dimensions and schematic views of new die stove are shown in Fig. 3 and Fig. 4. The new die stove is fabricated and installed at laboratory of Farm Machinery and Postharvest Technology Division, BRRI, Gazipur. To conduct the test run 10 kg of briquette was taken and cut into small pieces. The briquette pieces was placed on the grate of the stove and briquette was ignited. When the die barrel of the briquette machine got sufficient hot, the motor was started and husk was fed into the machine. After every 5 to 10 min four pieces of briquette was added to make stable heat in the stove. At the end of test run the remaining briquette was weighed and also the char remained in the stove was removed and quenched and weighed. Then the actual consumption of briquette fed into the stove was calculated by deducting the remaining amount and char. Deduction of char was adjusted by measuring the calorific value of briquette and char. Finally, the produced amount of briquette during the test run was weighed and necessary calculation was done to present the data.

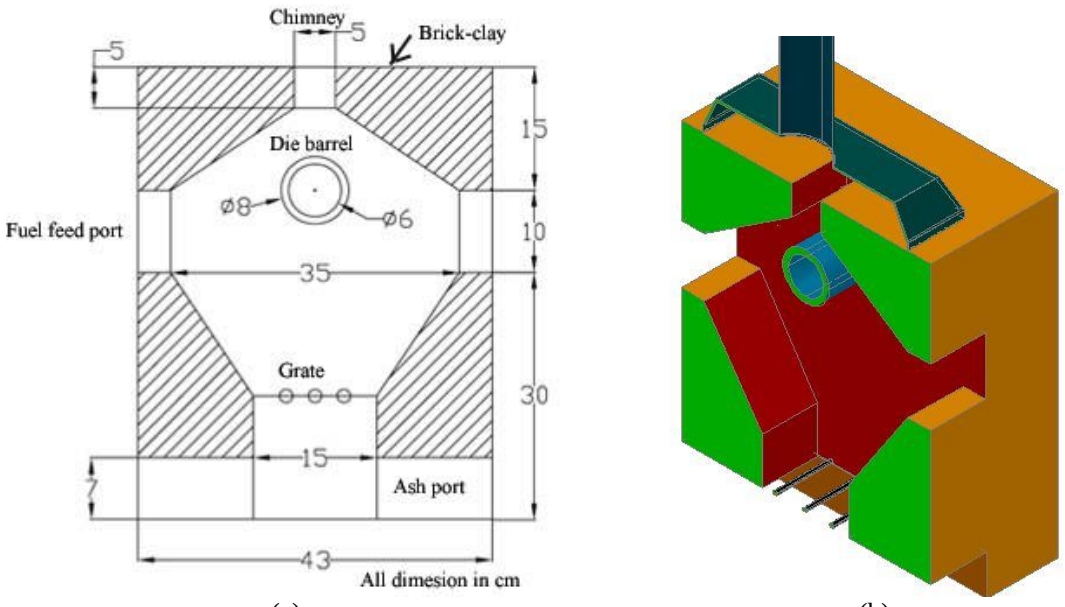

(a) (b)

Figure 3. (a) Cross sectional view of die-heating stove and 3D view of cross section of die-heating stove for briquetting machine

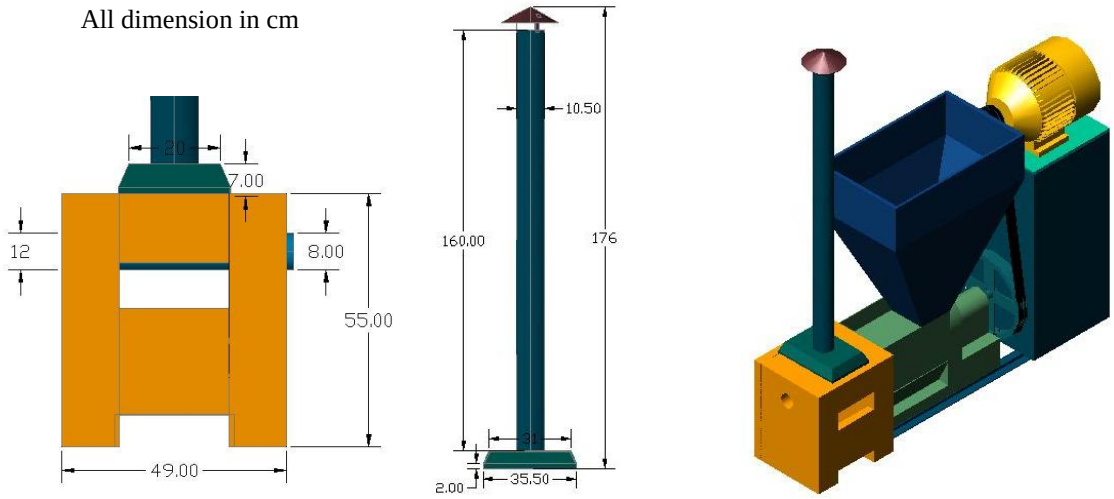

(a) (b) (c)

Figure 4. Overall dimension of die-stove (a) and chimney (b); and (c) isometric view of new setup

5. Results and Discussions

5.1 Stove performance

The photographic view of news setup of rice husk briquette machine of biomass stove and the produced briquette are shown in Fig 5. The test results of briquette production with die-stove fired by briquette are shown in Table 1. Three test runs were conducted. The average briquette production was found to be 88.87 kg/h. The consumption of briquette was found to be 75.77 kg/tonne of briquette produced. The electricity consumption by the motor was measured by a three phase digital energy meter and the average consumption was found to be 79.33 kWh/tonne of briquette produced. The results show that the electricity consumption by the briquette machine is reduced drastically compared to the previous results of electricity consumption with electric heater and motor as 152 kWh to 250 kWh/tonne. This shows a significant reduction of the electricity consumption by the briquette machine. Financial analysis and cost of CO_2 reduction analysis were done to check the viability of the new die-stove.

(a) (b)

Figure 5. (a) Showing briquette coming out from brick-clay die stove and (b) the briquette

Table 1. Rice husk briquette production with brick-clay die-heating stove

Run no.	Average die temperature, °C	Briquette production rate, kg/h	Briquette consumption in die stove, kg/tonne	Electricity consumption, kWh/tonne
1	372	86.2	75.6	82.6
2	398	92.7	79.4	76.5
3	380	87.7	72.3	78.9
Average	383.33	88.87	75.77	79.33

5.2 Financial analysis

Financial analysis is done based on the assumption of yearly briquette production (440 tonne/year [10]), life time of stove and electricity tariff. The cash flow analysis shows a negative net present value (NPV) at present electricity tariff (6 BDT/kWh) and briquette price (8.0 BDT/kg). Then a sensitivity analysis was done by varying the tariff of electricity. At a rate of 8.1 BDT/kWh tariff of electricity show positive NPV value and also the benefit cost ratio is to be 1.05.

Cost of CO_2 reduction analysis shows that at present rate of electricity tariff the CO_2 reduction is to be around US$25.0/tonne. High cost of CO_2 reduction is due to the comparison with a subsidized rate of electricity with high valued briquette fuel. The sensitivity analysis shows that the cost of CO_2 reduction is zero at 8.6 BDT/kWh of electricity.

6. Conclusion

Rice husk briquette is quite much popular as cooking fuel in Bangladesh. However, the production process of the briquette is electricity intensive. As an energy-starved country the use of electricity to commercially produce biomass briquette is questionable. However, the electricity consumption can be reduced by using a die-stove made of refractory clay-brick (instead electric-heater). With this technological change the electricity consumption is reduced by approximately 50% of the existing heated die screw extruder technology.

References

[1] Moral, M.N.A, and Rahman, A.N.M.M. (1999): Briquetting Activities in Bangladesh. Proceedings of Training Workshop on Renewable Energy Education and Application for Rural Communities in Bangladesh. Nov.27-Dec.03, 1999. Organized by Center for Energy Studies, Bangladesh University of Engineering and Technology, Dhaka, Bangladesh. pp.368-379.

[2] Dasgupta, N., Baqui, M. A., Dhingra S., Raman, P., Ahiduzzaman, M. And Kishore, V.V. N. (2003): Benefits of Improved Rice Husk Combustion, Bangladesh. NRI report no. 2764. p. 8, 21, 67.

[3] Ahiduzzaman, M. (2007). Rice Husk Energy Technologies in Bangladesh. Agricultural Engineering International: the CIGR Ejournal. Invited Overview No. 1. Vol. IX.

[4] UNEP (2009). Converting Waste Agricultural Biomass into a Resource. Compendium of Technologies. United Nations Environmnetal Programme, Division of Technology, Industry and Economics. International Environmental Technology Center, Osaka/Shiga, Japan.

[5] Islam, M. N. (1999): Non-Technical Issues on Application of Renewable Energy Technologies in Bangladesh. Proceedings of Training Workshop on Renewable Energy Education and Application for Rural Communities in Bangladesh. Nov. 27-Dec. 03. 1999. Dhaka, Bangladesh. Page.502.

[6] Grover, P.D. and Mishra, S.K. (1996) Biomass briquetting: Theory and Practices. RWEDP, Food and Agricultural Organization of the United Nations.

[7] Ahiduzzaman, M. (2006). Production and Use of Densified Biofuel in Mymensingh District (Bangladesh) under technical and Socio-economical Aspects. M.Sc. Thesis, Submitted to the Department of Sustainable Energy Systems and Management, University of Flensburg, Germany.

[8] Hardman, J.S. (2001): Briquetting of Rice Husk, and Production of Value-Added Products from Rice Husk. Progress Report of DFID Project-R7659 "Benefits from Improved Rice Husk combustion Efficiency. pp.3-6.

[9] Bhattacharya, S.C., Leon, M. A. and Rahman, M. M. (2002): A Study on Improved Biomass Briquetting. Energy for Sustainable Development. Volume VI, No. 2. pp.107,110. www.retsasia.ait.ac.th/Publications/ESD.pdf

[10] Ahiduzzaman, M. (2011) "Studies and Investigation on Extraction of Energy and Value-Added Product from Rice Husk", Ph.D. Thesis, Mechanical and Chemical Engineering Dept, Islamic University of Technology, Sept. 2011.

Available online at www.sciencedirect.com

SciVerse ScienceDirect

Procedia Engineering 00 (2012) 000–000

Procedia Engineering

www.elsevier.com/locate/procedia

5th BSME International Conference on Thermal Engineering

Corrosion of Magnesium and Aluminum in Palm Biodiesel: A Comparative Evaluation

K. V. Chew[a], A. S. M. A. Haseeb[a]*, H. H. Masjuki[a], M. A. Fazal[a], M. Gupta[b]

[a]*Department of Mechanical Engineering, University of Malaya, 50603 Kuala Lumpur, Malaysia*
[b]Department of Mechanical Engineering, National University of Singapore, 119260 Singapore

Abstract

The present study aims to investigate the comparative corrosion of light-weight metals such as aluminum and magnesium in palm biodiesel. Immersion test at room temperature for each metal was carried out for 1440 hours. Sample characterization techniques include weight loss measurement, scanning electron microscope (SEM), x-ray diffraction (XRD) and TAN (total acid number) analysis. Results showed that the corrosion rate of magnesium was much higher compared to that of aluminum at the same range of time. The surface morphology revealed a significant difference between the biodiesel exposed aluminum and magnesium specimens. Upon exposure in biodiesel, the magnesium surface was found to be fully covered by gel-like sticky mass which aluminum surface appears clean.

Keywords: Corrosion; magnesium; aluminum; biodiesel.

1. Introduction

As the automotive industries are approaching to address the environmental concerns, the problem of fuel consumption as well as weight reduction come to the fore. Therefore automobile researchers are now showing much interest for the metals of lighter weight with good cast-ability in order to improve the engine performance and reduce the energy consumption [1]. Over the last few years, light-weight non-ferrous metals such as Al, Mg are being increasingly used to replace the current heavy-weight cast iron blocks in manufacturing of different engine components [1-2]. Many automotive applications are also focused on thermal sprayed aluminum liners, metal-matrix composite in place of heavy metals [1-3]. Adaption of light materials resulted reduction of fuel consumption and at the same time provided better engine performance. The reported improvement in fuel consumption varies widely from 1.9-8.2% for every 10% reduction in vehicle weight [4-5]. Many of the engine components which are made from aluminum (piston, piston ring, cylinder, transmission etc.) [3] and magnesium (valve covers, cylinder head covers, housing, intake manifolds etc.) [6] come in contact with fuel. Study on the compatibility of these light weight components with the newly adapted and promising alternative fuel, biodiesel is a big issue to consider. This is because biodiesel is more corrosive compared to conventional petroleum diesel [7-8].

There are very limited number of studies reported on the corrosion of light weight metals such as aluminum and magnesium upon exposure to biodiesel. Corrosion study on aluminum piston in different biodiesels such as Jatropha Curcas, Karanja, Mahua and Salvadora was carried out by Kaul et al., [9]. They found that aluminum piston was more susceptible to corrosion in J.curcas and Salvadora biodiesel as compared to other biodiesel and diesel. Díaz-Ballote et al., [10] investigate

* Corresponding author. Tel.: +6-03-79675212; fax: +6-03-79675317.
E-mail address: haseeb@um.edu.my

the electrochemical corrosion behavior of aluminum exposed to various biodiesels at different stages of the washing process. It was reported that the corrosion characteristics of aluminum in biodiesel contaminated with alkalis is similar to the corrosion behavior of aluminum in aqueous solutions. In a couple of studies [11-12], it has been reported that aluminum is less corrosive in palm biodiesel as compared to other non-ferrous metals such as copper and brass. As a light-weight metal, magnesium is being considered as competitive to aluminum in automobile engine. It is approximately 35% lighter than aluminum yet it exhibits similar level of strength. A literature search on the fundamental corrosion study of magnesium in biodiesel has shown the scarcity of publications in this field. Therefore, there is a need to study the corrosion of magnesium in biodiesel and to gain comparative data on the corrosion of these light-weight metals, aluminum and magnesium. The aim of the present work is to compare the corrosion characteristics of aluminum and magnesium in palm biodiesel. Although both aluminum and magnesium are likely to be used in alloy form in automobile, commercially pure aluminum and magnesium are investigated in this work. The use of commercially pure form of both metals are expected to lead a basic understanding of the corrosion characteristics of those metals in biodiesel by avoiding complication imposed by alloying elements. Results obtained in the study will form a basic for further understanding of corrosion of perspective alloys in the future.

2. Materials and method

2.1 Materials and characteristics

The palm biodiesel used in this work was supplied by Mission Biotechnologies Sdn Bhd, Malaysia. The analysis report given by the supplier showed 98.8% ester content. Main impurities were free glycerol (~0.014 %), monoglyceride (~0.75%), diglyceride (~0.12%), triglyceride (~0.05%), glycerol (~0.23%), water (~275 ppm) and contamination (~2.71 ppm). The acid value of the investigated biodiesel was ~0.27 mgKOH/g. All specifications were within the limit given by EN 14214 standards. The Al alloy 5086 contains 95% Al, 3.86% Mg, 0.55% Fe, 0.99% Mn and 0.03% Si while the pure Mg sample contains 99.9% Mg, 0.01% Al, 0.04% Fe, 0.78 ppm Cr and 0.002 ppm Zn.

2.2 Experimental setup

Samples for immersion tests were prepared as follow. Aluminum and magnesium composed of 8 mm diameter and 2 mm thickness were prepared from respective rods by wire electrical discharge machining (WEDM). Each of the coupons was then ground mechanically by using abrasive paper from grade 600 to 2000. Two beakers were filled with 2 liters of biodiesel (B100) each. Static immersion test was done by holding the coupon with silk string to allow maximum surface exposure. Before immersion, the coupons were degreased with acetone and weighted in an electronic balance with ±0.01 mg accuracy. The prepared aluminum and magnesium coupons were then hung separately in two separate beakers. All beakers were covered by a watch glass to prevent foreign particles from entering. Experiment was conducted at room temperature. Upon immersion for 720 h and 1440 h, three coupons and 60 ml of biodiesel were taken out from each beaker. Residue that formed on the magnesium surface was collected by drying in vacuum oven for 24 hours at 27^{o}C. The rest of the coupons were cleaned by brushing with soft toothbrush in the running deionized water to remove lose corrosion product. Then it was degreased with acetone and weight loss is measured.

2.3 Corrosion analysis

The surface morphologies and chemical states of the corroded surface were examined under a scanning electron microscope (SEM) and X-ray diffraction machine (XRD). The XRD analysis was performed using a diffractometer with a Cu Kα radiation of wavelength of 1.5406 Å operated at 45kV/30mV. At incident angle 1.0, the samples were step-scanned from position 30˚ to 90˚ with a step size of 0.1 and a step time of 1 second. The changes in acidity of the biodiesel were analyzed by total acid number (TAN) analyzer as per ASTM D664. Quantitative analysis of metals corrosion was done according to the following equation 1.

$$Corrosion\ rate\ \left(mpy\right) = \frac{534\,w}{d\ t\ A} \tag{1}$$

where corrosion rate, mpy stands for milli-inch per year (1 mpy = 0.0254 mm/year); w: weight loss in mg; *d*: density in g/cm^3, A: area of sample in square inch; and t: exposed time in h.

3. Results and discussion

Fig. 1 shows the corrosion rate of aluminum and magnesium immersed in B100 for 720 h and 1440 h at room temperature. Corrosion rates for pure aluminum at 720 h and 1440 h are 0.1230 mpy and 0.0527 mpy respectively. Corrosion rates for magnesium are much higher which are 3.0910 mpy at 720 h and 2.6563 mpy at 1440 h.

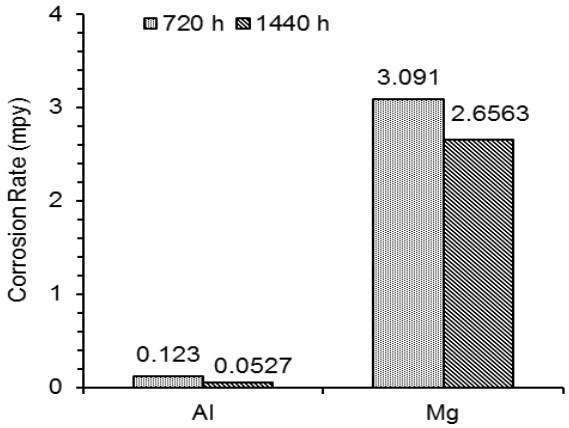

Fig. 1. Corrosion rate of aluminum and magnesium (Mg) in palm biodiesel for different immersion time.

It is seen that the corrosion rate of both metals decrease with time. Fazal et al., [12] also observed that corrosion of aluminum slightly decreases with immersion time. It is clear that magnesium exhibits higher corrosion rate compared to aluminum. This is thought to be due to the higher reactivity of magnesium. Magnesium is less noble compared to aluminum in the galvanic series where it prompts to anodic reaction.

Fig. 2 shows the appearance of aluminum and magnesium coupons after the immersion test for 720 h and 1440 h. There is a distinct difference with appearance of the two metals. Magnesium coupon is seen to be covered by gel-like mass, which aluminum surface appears clean. This gel-like mass is yellowish in color and is highly sticky in nature. It behaves like a gum and is not easy to be removed by rubbing. The extent of gum formation is higher at longer immersion time. Formation of sediment and gum may cause engine performance problem including fuel filter plugging [13]. Further investigations were carried out on the gum which will be discussed later.

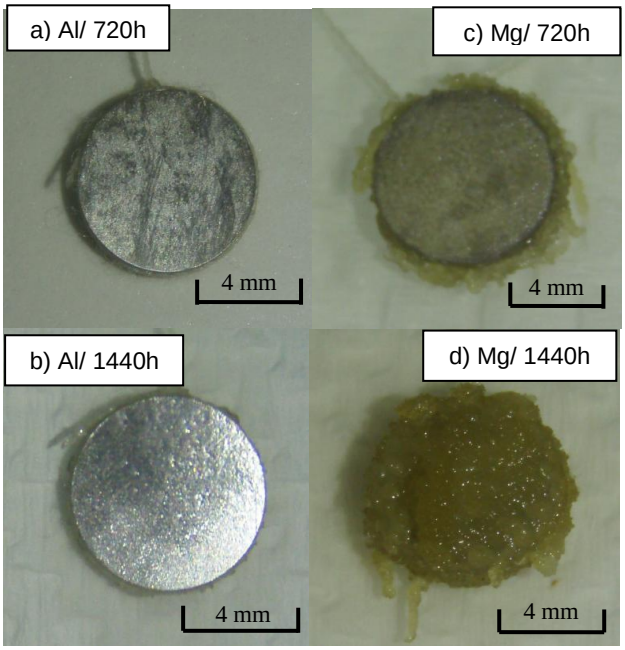

Fig. 2. Optical photographs of aluminum (a-b) and magnesium (c-d) surfaces after exposure to biodiesel at room temperature for 720 h and 1440 h.

Samples upon exposure were cleaned with soft toothbrush in running deionized water and ultrasonically degreased with acetone for 5 minutes. The SEM images of aluminum and magnesium immersed in B100 for 1440 h at room temperature are shown in Fig. 3. At X1000 magnification, the grinding lines on the as-received coupons are clearly seen in both metals. It is observed that upon 1440 h exposure, the surface of aluminum did not undergo any significant changes. The grinding lines are still clearly visible as before. However, the surface morphology of the magnesium coupon changed significantly. Corrosion attack caused a roughing of the surface. Round pits of about 5µm diameter are visible on the surface. Corrosion attack appears to be rather uniform.

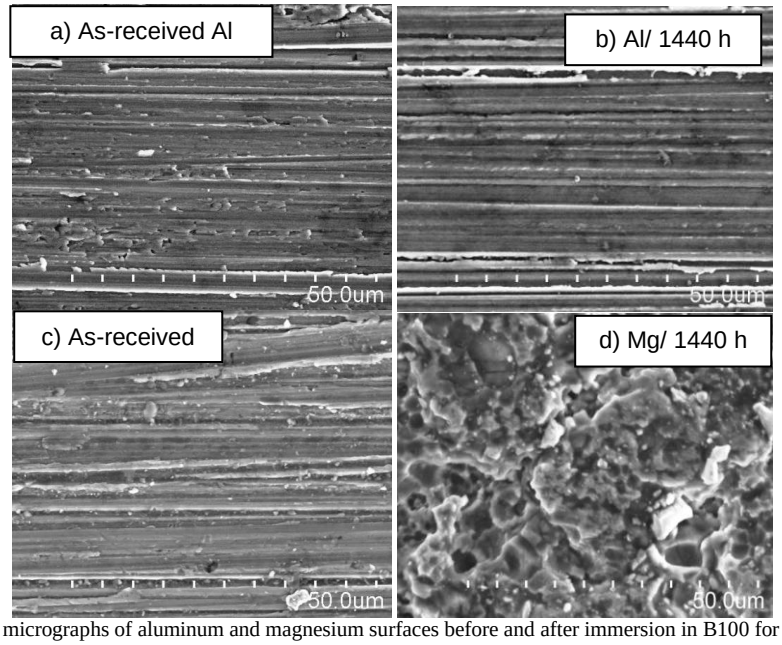

Fig. 3. SEM micrographs of aluminum and magnesium surfaces before and after immersion in B100 for 1440 h at room temperature.

Fig. 4 shows the XRD analysis on the surface of aluminum and magnesium after immersion test for 1440 h. XRD analysis was carried out with 1.0 incident angle, position from 30˚ to 90˚ and step size of 0.1. All the peaks show that there is no oxide form on the aluminum and magnesium surface. Peaks belonging only to the metallic state are visible for both metals. XRD pattern do not reveal the existence of any compound formed as corrosion products. This suggests that any corrosion product that might have formed on the surface of both metals are not thick enough to be detected by the XRD technique. It has been seen earlier that the corrosion rate of both metals decreases slightly with immersion time. This indicates the possibility of the formation of some sort of protective layer on the metals. However, this layer appears to be too thin to be detected by XRD. Further investigations by surface analytical technique are planned for future.

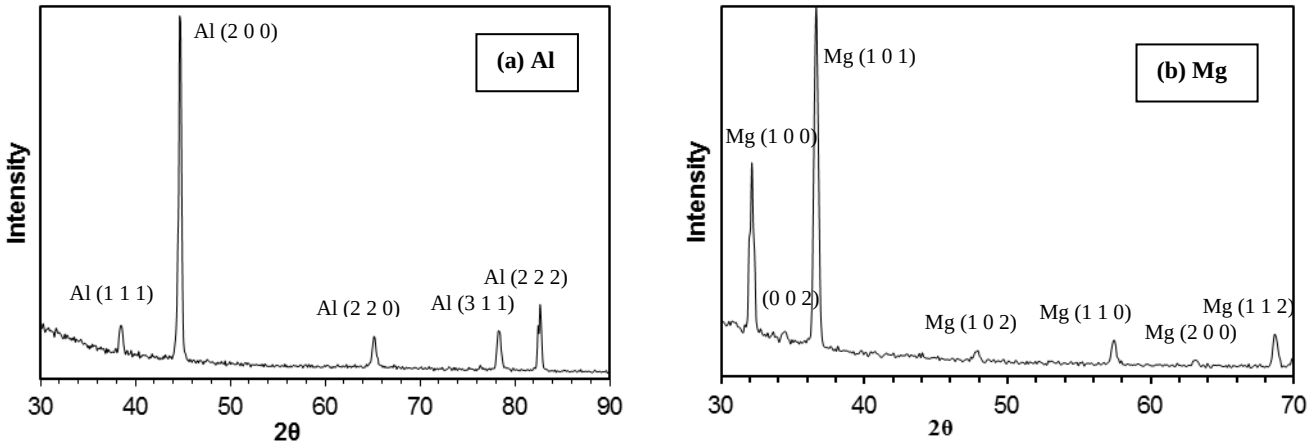

Fig. 4. XRD patterns of (a) aluminum (Al) and (b) magnesium (Mg) surface after exposure in B100 for 1440 h.

After the immersion test, the biodiesel sample was characterized by TAN value measurement. The results are shown in Fig. 5. According to ASTM D6571, the limit for TAN in biodiesel is 0.5 mgKOH/g. The as-received biodiesel falls within this limit which is 0.27 mgKOH/g. However, upon exposure to aluminum and magnesium for 1440 h at room temperature, the TAN value increases significantly to 0.92 mgKOH/g and 0.87 mgKOH/g respectively.

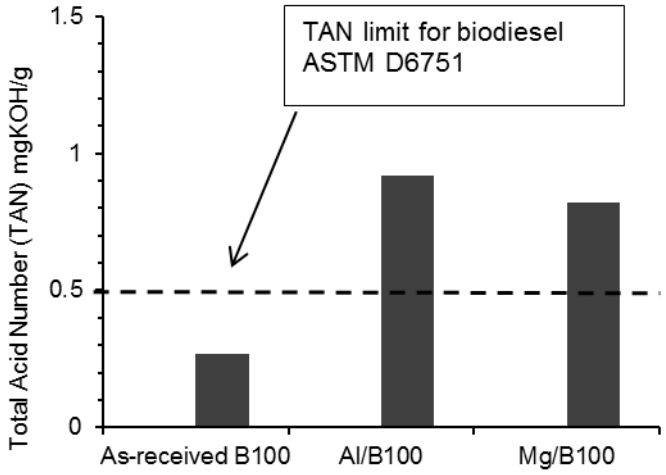

Fig. 5. Total acid number (TAN) of biodiesel before and after exposure to Al and Mg for 1440 h.

The increase of TAN value indicates that the biodiesel has been degraded [14]. The degradation process is due to the oxidation of the unsaturation in the oil with the presence of metal [9]. The oxidation process leads to formation of acids, ketones, aldehydes, lactones, alkylofurances etc. [15]. The increased in TAN values is similar for both metals, although their corrosion rates differ significantly. This suggests that there is no strong correlation between TAN number and corrosion rate.

4. Conclusions

This study suggests the following conclusion:

i. Magnesium exhibits much higher corrosion rate in biodiesel compared to that of aluminum.
ii. The surface morphology of biodiesel exposed magnesium coupon changed significantly while aluminum did not undergo any significant changes. Upon exposure in biodiesel, round pits of about 5μm diameter are visible on the magnesium surface while the grinding lines are still clearly visible on aluminum surface as before.
iii. No oxide or other corrosion product could be detected on aluminum and magnesium by XRD. This suggests that any corrosion product that might have formed on the surface of both metals is not thick enough to be detected by the XRD technique.
iv. Biodiesel undergoes significant degradation upon exposure to metals. It crosses the TAN limit of 0.5 mgKOH/g.
v. Magnesium surface is seen to be covered by yellowish gel-like sticky mass, which aluminum surface appears clean. This suggests that magnesium catalysts the oxidation and polymerization reaction in biodiesel to form gum on magnesium surface.

Acknowledgement:

The author would like to acknowledge the financial support provided by the Ministry of Science, Technology & Innovation (MOSTI) under the science Fund by Grant No: 03-02-03-SF3073, University of Malaya Research Grant (UMRG) by Project No.: RG137-12AET and by the Institute of Research Management and Consultancy, University of Malaya (UM) under the PPP Project No: PS118/2010B.

References

[1] Du, J.D., Han, W.J., Peng, Y.H., Gu, C.C., 2012. Potential for reducing GHG emissions and energy consumption from implementing the aluminum intensive vehicle fleet in China, Energy 35, p. 4671.
[2] Hakamada, M., Furuta, T., Chino, Y., Chen, Y., Kusuda, H., Mabuchi, M., 2007. Life cycle inventory study on magnesium alloy substitution in vehicles, Energy 32, p. 1352.
[3] Tung, S.C., McMillan M.L., 2004. Automotive tribology overview of current advances and challenges for the future, Tribology International 37, p. 517.
[4] Wohlecker, R., Johannaber, M., Espig, M., 2007. Determination of Weight Elasticity of Fuel Economy for ICE, Hybrid and Fuel Cell Vehicles, 2007 SAE World Congress, 2007 Detroit, Michigan. SAE International, SAE Paper No. 2007-01-0343.
[5] Pagerit, S., Sharer, P., Rousseau, A., 2006. Fuel Economy Sensitivity to Vehicle Mass for Advanced Vehicle Powertrains, SAE 2006 World Congress 2006, Detroit, Michigan. SAE International, SAE Paper No. 2006-01-0665.
[6] Blawert, C., Hort, N., Kainer, K.U., 2004. Automotive applications of magnesium and Its alloys, Transactions of the Indian Institute of Metals 57, p. 397.
[7] Fazal, M.A., Haseeb, A.S.M.A., Masjuki, H.H., 2011. Biodiesel feasibility study: An evaluation of material compatibility; performance; emission and engine durability, Renewable and Sustainable Energy Reviews 15, 1314.
[8] Fazal, M.A., Haseeb, A.S.M.A., Masjuki, H.H., 2011. Effect of temperature on the corrosion behavior of mild steel upon exposure to palm biodiesel. Energy 36, 3328.
[9] Kaul, S., Saxena, R.C., Kumar, A., Negi, M.S., Bhatnagar, A.K., Goyal, H., Gupta, A. K., 2007. Corrosion behavior of biodiesel from seed oils of Indian origin on diesel engine parts, Fuel Processing Technology 88, 303.
[10] Díaz-Ballote, L., López-Sansores, J.F., Maldonado-López, L., Garfias-Mesias, L.F., 2009. Corrosion behavior of aluminum exposed to a biodiesel, Electrochemistry Communications 11, 41.
[11] Fazal, M.A., Haseeb, A.S.M.A., Masjuki, H.H., 2012. Degradation of automotive materials in palm biodiesel. Energy 40, 76.
[12] Fazal, M.A., Haseeb, A.S.M.A., Masjuki, H.H., 2010. Comparative corrosive characteristics of petroleum diesel and palm biodiesel for automotive materials, Fuel Processing Technology 91, 1308.
[13] Monyem, A., Van Gerpen, J.H., 2001. The effect of biodiesel oxidation on engine performance and emissions, Biomass and Bioenergy 20, 317.
[14] Fazal, M.A., Haseeb, A.S.M.A., Masjuki, H.H., 2011. Effect of different corrosion inhibitors on the corrosion of cast iron in palm biodiesel, Fuel Processing Technology 92, 2154.
[15] Niczke, L., Czechowski, F., Gawel, I., 2007. Oxidized rapeseed oil methyl ester as a bitumen flux: Structural changes in the ester during catalytic oxidation. Progress in Organic Coatings 59, 304.